

Absolute linear instability in laminar and turbulent gas/liquid two-layer channel flow

By LENNON Ó NÁRAIGH¹, PETER D. M. SPELT²
AND STEPHEN J. SHAW³

¹School of Mathematical Sciences, University College Dublin, Belfield, Dublin 4, Ireland

²Département Mécanique, Université de Lyon 1 and Laboratoire de la Mécanique des Fluides & d'Acoustique (LMFA), CNRS, Ecole Centrale Lyon, Ecully, France

³Department of Mathematical Science, Xi'an Jiaotong-Liverpool University, 111 Ren Ai Road, Dushu Lake Higher Education Town, Suzhou, Jiangsu, 215123, China.

(Received May 17, 2021)

We study two-phase stratified flow where the bottom layer is a thin laminar liquid and the upper layer is a fully-developed gas flow. The gas flow can be laminar or turbulent. To determine the boundary between convective and absolute instability, we use Orr–Sommerfeld stability theory, and a combination of linear modal analysis and ray analysis. For turbulent gas flow, and for the density ratio $r = 1000$, we find large regions of parameter space that produce absolute instability. These parameter regimes involve viscosity ratios of direct relevance to oil/gas flows. If, instead, the gas layer is laminar, absolute instability persists for the density ratio $r = 1000$, although the convective/absolute stability boundary occurs at a viscosity ratio that is an order of magnitude smaller than in the turbulent case. Two further unstable temporal modes exist in both the laminar and the turbulent cases, one of which can exclude absolute instability. We compare our results with an experimentally-determined flow-regime map, and discuss the potential application of the present method to non-linear analyses.

1. Introduction

We investigate linear absolute and convective instability for a liquid film sheared by laminar and turbulent gas streams in a channel. In the oil/gas industries, this approach serves as a model that can be used to predict the onset of droplet entrainment (Hall-Taylor & Hewitt 1970). The motivation for this work is twofold: previous work on the turbulent case focussed uniquely on temporal stability analysis (Miesen & Boersma 1995; Boomkamp & Miesen 1996; Boomkamp *et al.* 1997; Özgen *et al.* 1998), while previous work on the laminar case (Valluri *et al.* 2010) omitted large regions of parameter space that are relevant to the oil-and-gas industries, and which are found herein to be absolutely unstable. The current work aims to fill in these two gaps in the literature and introduces modifications and extensions of existing methodologies (developed previously for single-phase flows or for temporal stability analysis only) that are potentially of interest in other areas.

The route to droplet entrainment from a liquid layer into a gas stream in pipe and channel flows is still unclear. The idealized system of fully-developed flow with a flat gas/liquid interface is linearly unstable to infinitesimally small perturbations. For a laminar base state, a stratification in dynamic viscosity produces instability; for a turbulent base state, the mechanism of Miles (1957) may also dominate for deep liquid layers at

large Froude numbers (Ó Náraigh *et al.* 2011*b*). Other mechanisms, such as a Tollmien–Schlichting mode in the liquid (Boomkamp & Miesen 1996) may also be important in certain parameter regimes. Although linear (temporal) instability is arguably a necessary condition for droplet entrainment in the gas, it does not provide much insight regarding whether a localized disturbance grows whilst it is merely convected downstream or whether instead the disturbance destabilizes the entire system. To answer these questions a spatio-temporal analysis is required. A recent spatio-temporal analysis by Valluri *et al.* (2010) has revealed a region in parameter space wherein the laminar base state is absolutely unstable, indicating that the system does not merely act as an amplifier but also as a generator of disturbances. This was found to include a large range of practically useful viscosity ratios, but was limited to a density ratio of $O(1)$.

The laminar density-matched problem studied by Valluri *et al.* (2010) has only limited applicability in oil/gas transport, where the density ratio is large, and where the operating conditions produce turbulence in the gas layer, or in both layers (see, e.g., the visualisation of droplet entrainment events by Lecoeur *et al.* (2010)). The present study therefore investigates the corresponding problem for a turbulent base state, but the laminar case is also revisited. Although replacement of the base state by a turbulent one (Ó Náraigh & Spelt 2010; Ó Náraigh *et al.* 2011*a*) in a linear modal spatio-temporal analysis may seem trivial, the results turn out to be difficult to interpret, due to the presence of multiple unstable modes. Therefore, in this study, we have developed a twin-track approach, in which modal analysis and ray analysis are combined to locate and characterize absolute instability. The ray analysis used herein extends the work of Delbende *et al.* (1998) for single-phase flows. This approach yields surprising results. In particular, it has revealed significant regions in parameter space where the turbulent base state is absolutely unstable for large density ratios. This also holds for the laminar base state, thereby contradicting Valluri *et al.* (2010), who only found absolute instability for density ratios of $O(1)$. We have therefore revisited the spatio-temporal work of Valluri *et al.* (2010), and have established using both ray and modal analyses that the laminar system is indeed absolutely unstable at large density ratios for a substantial range of viscosity ratios and liquid-film depths. Reasons for the oversight in the previous work are given.

The paper is organized as follows. The turbulence model and the linear stability analysis are formulated in Section 2. We discuss some theoretical and numerical aspects of the linear stability analysis in Section 3, paying close attention to the development of a ray analysis for two-phase flows. We apply this technique to the turbulent base state in Section 4, while the laminar case is revisited in Section 5. In Section 6 we argue for the importance of using the ray analysis and the modal analysis simultaneously, for complete and accurate results. We also compare the flow-regime boundaries identified herein with those found in experiments, and discuss the generalisation of our work to non-linear and non-parallel flows.

2. Linear stability analysis

In this section we review a model of turbulent channel flow used elsewhere by the authors (Ó Náraigh & Spelt 2010; Ó Náraigh *et al.* 2011*a*). This is a Reynolds-averaged model describing co-current flow in a stably-stratified system where the upper layer is a turbulent gas and the lower layer a laminar liquid film. We also recall the Orr–Sommerfeld technique used to determine the stability of the interface in this two-layer system. For reference, typical values of the problem parameters are given in Table 1, where the subscripts G, L indicate the gas and liquid, respectively.

Physical Quantity	Symbol	Numerical value
Gas-layer dynamic viscosity	μ_G	$1.8 \times 10^{-5} \text{ Pa} \cdot \text{s}$
Liquid-layer dynamic viscosity	μ_L	
Viscosity ratio	$m = \mu_L/\mu_G$	50–10000
Gas-layer density	ρ_G	1 kg m^{-3}
Liquid-layer density	ρ_L	
Density ratio	$r = \rho_L/\rho_G$	10^3
Liquid film thickness	d_L	$10^{-3}\text{--}10^{-2} \text{ m}$
Gas-layer depth	d_G	
Ratio of layer depths	$\epsilon = d_L/d_G$	0.01–0.2
Acceleration due to gravity	g	9.8 m s^{-2}
Surface tension	γ	0.07 N m^{-1}

TABLE 1. Table of parameters in the two-phase problem and their typical values. The range of values of the liquid-layer dynamic viscosity μ_L , the liquid-layer density ρ_L , and the liquid-film thickness d_L can be backed out from the gas-layer analogues and the ratios m , r , and ϵ , respectively.

2.1. The base state

We consider a flat-interface base state in two-layer stratified flow (Figure 1). The bottom layer is a thin, laminar, liquid layer, and the top layer is gaseous, turbulent and fully-developed. A pressure gradient is applied along the channel. The base-state profile of the system is a uni-directional flow in the horizontal, x - direction as a function of the cross-flow coordinate z . In the bottom layer, the profile is determined by balancing the viscous and the pressure forces; in the top layer, the viscosity in the balance law must be supplemented by the turbulent eddy viscosity:

$$\mu_G \frac{\partial U_0}{\partial z} + \tau_0 = \tau_1 + \frac{dP}{dL} z, \quad (2.1)$$

where $U_0(z)$ is the base-state velocity in the gas, τ_1 is the interfacial shear stress, and dP/dL is the applied pressure gradient. Moreover, $\tau_0 = -\rho_G \langle u'w' \rangle$ is the turbulent shear stress due to the averaged effect of the turbulent fluctuating velocities, u' and w' . In channel flows, it is appropriate to model this term using an eddy-viscosity model (Monin & Yaglom 1971). In mixing-length theory, the eddy viscosity depends on the local rate of strain (Bradshaw 1974), which means that the turbulent shear stress depends on the square of the rate of strain. Instead, as in the work of Ó Náraigh *et al.* (2011a) and Biberg (2007), we use an interpolation function for the eddy viscosity. This mimics the ordinary mixing-length theory near the interface and near the wall, and transitions smoothly from the near-wall and near-interfacial regions to the zone surrounding the gas centreline. Thus, the turbulent shear stress is linear in the rate of strain, and

$$\tau_0 = \mu_T \frac{\partial U_0}{\partial z}, \quad \mu_T = \kappa \rho_G d_G U_{*w} \mathcal{F}(s) \psi_1(s) \psi_w(1-s), \quad s = z/d_G, \quad (2.2)$$

where μ_T is the eddy viscosity and κ is the von Kármán constant, taken as 0.4. Additionally, U_{*w} is the friction velocity at the upper wall. The corresponding stress is τ_w , with $U_{*w} = \sqrt{|\tau_w|/\rho_G}$. Similarly, the interfacial friction velocity is defined as $U_* = \sqrt{\tau_1/\rho_G}$. The function \mathcal{F} is the interpolation function described in Ó Náraigh & Spelt (2010)

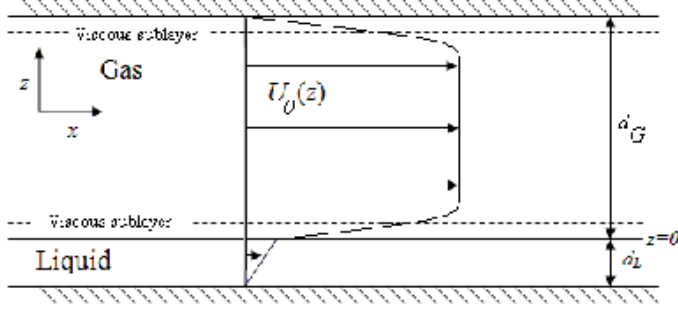


FIGURE 1. A schematic diagram of the base flow. The liquid layer is laminar, while the gas layer exhibits fully-developed turbulence, described here by a Reynolds-averaged velocity profile. A pressure gradient in the x -direction drives the flow.

and Ó Náraigh *et al.* (2011a):

$$\mathcal{F}(s) = s(1-s) \left[\frac{s^3 + |R|^{5/2} (1-s)^3}{R^2 (1-s)^2 + Rs(1-s) + s^2} \right], \quad R = \tau_i/\tau_w. \quad (2.3)$$

Finally, ψ_i and ψ_w are interface and wall functions respectively, which damp the effects of turbulence to zero rapidly near the interface and the wall. These are given below.

We non-dimensionalize the problem on the gas-layer depth d_G , the gas-layer density ρ_G , the gas-layer viscosity μ_G , and the velocity scale U_p , where

$$\rho_G U_p^2 = d_G |dP/dL|.$$

Then, integration of Equation (2.1) yields the non-dimensional base state:

$$U_0(z) = \begin{cases} \frac{\mu_G}{\mu_L} \left[-\frac{1}{2} Re (z^2 - \epsilon^2) + \frac{Re_*^2}{Re} (z + \epsilon) \right], & -\epsilon \leq z \leq 0, \\ \frac{\mu_G}{\mu_L} \left(\frac{1}{2} \epsilon^2 Re + \epsilon \frac{Re_*^2}{Re} \right) + \frac{Re_*^2}{Re} \int_0^z \frac{\left(1 - \frac{Re_*^2}{Re} s\right) ds}{1 + \frac{\kappa Re_*}{\sqrt{|R|}} g(s) \psi_i(s) \psi_w(1-s)}, & 0 \leq z \leq 1, \end{cases} \quad (2.4)$$

where $\epsilon = d_L/d_G$, $Re = \rho_G U_p d_G / \mu_G$, and where $Re_* = (U_*/U_p) Re$. Knowledge of Re_* amounts to knowledge of the interfacial shear stress. This is not known *a priori* as a function of the externally-imposed parameters. However, it is available within the model, and the root-finding procedure

$$U_0(1; Re_*) = 0 \quad (2.5)$$

yields Re_* as a function of the parameters $(Re, \epsilon, \mu_L/\mu_G)$. For completeness, we also list the interfacial and wall functions:

$$\psi_i(s) = 1 - e^{-C_A Re_*^2 s^2}, \quad (2.6a)$$

$$\psi_w(s) = 1 - e^{-C_A Re_*^2 s^2 / R^2}, \quad (2.6b)$$

where C_A is a constant fixed such that the interfacial and wall viscous sublayers are five wall-units in extent (Pope 2000). The functional forms for \mathcal{F} and the wall functions are confirmed by the excellent agreement between the model predictions of the base state and experiments and numerical simulation (Ó Náraigh *et al.* 2011a). Having constituted the base state, we now introduce the theory necessary to determine its stability.

2.2. The perturbation equations

We base the dynamical equations for the interfacial motion on the Reynolds-averaged Navier–Stokes (RANS) equations. The turbulent velocity is decomposed into averaged and fluctuating parts. We make the quasi-laminar approximation, which means that the fluctuations are only considered in the base state, where they are modelled using the eddy viscosity (Section 2.1). Before deriving equations for perturbations induced by small waves at the interface, we discuss the dynamics of these perturbations with respect to their interactions with the turbulent eddies in the flow.

In a realisation of the three-dimensional turbulent two-layer flow with small-amplitude waves, a Fourier mode decomposition can be made of the interface elevation and field variables. Here, ensemble-averaged Fourier modes are assumed to be predominantly two-dimensional. The correspondingly averaged equations of motion are linearized in terms of wave amplitude. The linearized problem contains wave-induced Reynolds stress terms (WIRs), but these have been found recently not to be significant in two-layer flows such as those studied here (Ó Náraigh *et al.* 2011*a,b*). This can also be seen from an order-of-magnitude estimate of the WIRs terms compared to inertial terms in the perturbation momentum equation. Further theoretical justification exists for the case of viscosity-contrast instability, where the instability is dominated by conditions close to the interface, a zone where the perturbation turbulent stresses are damped rapidly to zero by the existence of viscous sublayers. In practical terms, the quasi-laminar approximation, wherein the WIRs are ignored and the effect of turbulence is assumed to be entirely through the base-state velocity profile, while brutal in its simplicity, yields similar results to other turbulence models that explicitly include the WIRs. It also predicts critical Reynolds numbers for the onset of wavy flow that agree with the laboratory experiments of Cohen & Hanratty (1965) and Craik (1966). The reader is referred to the papers by Ó Náraigh *et al.* (2011*a,b*) for further details.

Here, we study linear spatio-temporal instability. Although the above-mentioned prior findings are limited to temporal Fourier modes, there is an analytical connection between spatio-temporal and temporal modes (Ó Náraigh *et al.* 2012) (see also Appendix A), such that the properties of the temporal study are inherited by the spatio-temporal one. Therefore, we make here also the quasi-laminar approximation. Thus, a small disturbance $z = \eta(x, t)$ centred around the flat interface $z = 0$ gives rise to disturbances in the velocity and pressure fields, which satisfy the following linearized equations of motion in the j^{th} phase ($j = L, G$):

$$r_j \left[\frac{\partial}{\partial t} \delta u + U_0 \frac{\partial}{\partial x} \delta u + \frac{dU_0}{dz} \delta w \right] = -\frac{\partial}{\partial x} \delta p + \frac{m_j}{Re} \left(\frac{\partial^2}{\partial x^2} + \frac{\partial^2}{\partial z^2} \right) \delta u, \quad (2.7a)$$

$$r_j \left[\frac{\partial}{\partial t} \delta w + U_0 \frac{\partial}{\partial x} \delta w \right] = -\frac{\partial}{\partial z} \delta p + \frac{m_j}{Re} \left(\frac{\partial^2}{\partial x^2} + \frac{\partial^2}{\partial z^2} \right) \delta w, \quad (2.7b)$$

$$\frac{\partial}{\partial x} \delta u + \frac{\partial}{\partial z} \delta w = 0, \quad (2.7c)$$

where $(r_L, r_G) = (r, 1)$ and $(m_L, m_G) = (m, 1)$. Using the incompressibility condition, this system of equations reduces to a single equation in the streamfunction ϕ . Further simplification occurs when the streamfunction is written as a sum of normal modes:

$$\phi(x, z, t) = \frac{1}{2\pi} \int_{C_\alpha = \mathbb{R}} d\alpha e^{i\alpha x} \phi_\alpha(z, t), \quad (2.8)$$

which in turn can be written in Laplace-transform notation:

$$\phi(x, z, t) = \frac{1}{4\pi^2} \int_{C_\alpha} d\alpha \int_{C_\omega} d\omega e^{i(\alpha x - \omega t)} \phi_{\alpha\omega}(z), \quad (2.9)$$

where C_ω is the Bromwich contour (Arfken & Weber 2001). If the ω -singularities in the function $\phi_{\alpha\omega}(z)$ lie below the real axis in the complex- ω plane, then the integral (2.9) is an ordinary double Fourier integral. Using the Fourier and Laplace decompositions, Equations (2.7) reduce to the Orr-Sommerfeld equation:

$$i\alpha r_j \left[\left(U_0 - \frac{\omega}{\alpha} \right) (D^2 - \alpha^2) \phi_{\alpha\omega} - \frac{d^2 U_0}{dz^2} \phi_{\alpha\omega} \right] = \frac{m_j}{Re} (D^2 - \alpha^2)^2 \phi_{\alpha\omega}, \quad (2.10)$$

where $D = d/dz$. Equation (2.10) only holds in the interior parts of the domain, $z \in (-\epsilon, 0^-) \cup (0^+, 1)$. To close the Equation (2.10), no-slip and no-penetration conditions are applied at $z = -\epsilon$ and $z = 1$:

$$\phi_{\alpha\omega}(-\epsilon) = D\phi_{\alpha\omega}(-\epsilon) = \phi_{\alpha\omega}(1) = D\phi_{\alpha\omega}(1) = 0, \quad (2.11)$$

and the streamfunction is matched across the interface $z = 0$, where the following conditions hold (we use the notation $c = \omega/\alpha$):

$$\phi_L = \phi_G, \quad (2.12a)$$

$$D\phi_L = D\phi_G + \frac{\phi_G}{c - U_0} \left(\frac{dU_0}{dz} \Big|_{0^+} - \frac{dU_0}{dz} \Big|_{0^-} \right), \quad (2.12b)$$

$$m(D^2 + \alpha^2)\phi_L = (D^2 + \alpha^2)\phi_G, \quad (2.12c)$$

$$\begin{aligned} m(D^3\phi_L - 3\alpha^2 D\phi_L) + i\alpha r Re(c - U_0) D\phi_L + i\alpha r Re \frac{dU_0}{dz} \Big|_{0^-} \phi_L - \frac{i\alpha r Re}{c - U_0} (F + \alpha^2 S) \phi_L \\ = (D^3\phi_G - 3\alpha^2 D\phi_G) + i\alpha r Re(c - U_0) D\phi_G + i\alpha r Re \frac{dU_0}{dz} \Big|_{0^+} \phi_G. \end{aligned} \quad (2.12d)$$

Here F and S denote parameters that encode the effects of gravity and surface tension, respectively; they are defined here for the first time as

$$F = \frac{gd_G}{(\mu_G/\rho_G d_G)^2} \frac{r-1}{Re^2} := F_0(r-1)/Re^2, \quad (2.13)$$

$$S = \frac{\gamma}{\mu_G^2/\rho_G d_G} \frac{1}{Re^2} := S_0/Re^2, \quad (2.14)$$

where g is acceleration due to gravity and γ is surface tension. The appropriate range of values for F_0 and S_0 is discussed in Sec. 4. We abbreviate the Orr-Sommerfeld (or OS) equation (2.10) and the matching conditions (2.11)–(2.12) using operator notation,

$$\mathcal{L}_{\alpha\omega}\phi_{\alpha\omega} = i\omega\mathcal{M}_{\alpha\omega}\phi_{\alpha\omega}. \quad (2.15)$$

This equation amounts to an eigenvalue equation, which we solve numerically by introducing a trial solution:

$$\phi_{\alpha\omega}(z) \approx \sum_{n=0}^{N_1} a_n T_n \left(\frac{2z}{\epsilon} + 1 \right), \quad -\epsilon \leq z \leq 0, \quad (2.16a)$$

$$\phi_{\alpha\omega}(z) \approx \sum_{n=0}^{N_2} b_n T_n(2z-1), \quad 0 \leq z \leq 1, \quad (2.16b)$$

where $T_n(\cdot)$ is the n^{th} Chebyshev polynomial. We substitute Equation (2.16) into Equation (2.15) and evaluate the result at $N_1 + N_2 - 6$ interior points. The ansatz (2.16) is also substituted into the eight boundary and interfacial conditions. This yields $N_1 + N_2 + 2$ linear equations in as many unknowns. In matrix terms, we have to solve

$$L_{\alpha\omega}\mathbf{v} = i\omega M_{\alpha\omega}\mathbf{v}, \quad (2.17)$$

where $\mathbf{v} = (a_0, \dots, a_{N_1}, b_0, \dots, b_{N_2})^T$. Such an equation is readily solved using linear-algebra packages. This method is described in more detail and its implementation is tested against benchmarks in another paper by the present authors (Valluri *et al.* 2010). The number of collocation points ($N_1 + 1, N_2 + 1$) is adjusted until convergence is achieved. The application of this numerical method will be the subject of the following sections.

3. Further numerical methods and postprocessing

In this section we revisit the basic definition of absolute instability, namely that the streamfunction response to a localized disturbance should grow exponentially in time at the origin of the disturbance. Solving the associated Cauchy problem gives a quick and clear method to characterize the instability. This approach also enables us to pinpoint the source of the instability through an energy-budget analysis. We also review herein an equivalent method to determine absolute instability, namely modal analysis.

3.1. Modal analysis

A purely temporal analysis involves the solution of the eigenvalue problem (2.15), where we write $\alpha = \alpha_r + i\alpha_i$, $\omega = \omega_r + i\omega_i$, for $\alpha = \alpha_r$ only. This gives a dispersion relation

$$(\omega_i^{\text{temp}}(\alpha_r), \omega_i^{\text{temp}}(\alpha_r)) = (\omega_r(\alpha_r, \alpha_i = 0), \omega_i(\alpha_r, \alpha_i = 0)),$$

with associated group velocity $c_g = d\omega_i^{\text{temp}}/d\alpha_r$. The pair $(\alpha_r, \omega_i^{\text{temp}}(\alpha_r))$ that maximizes ω_i is called the *most dangerous mode*. The flow is linearly unstable if $\omega_i^{\text{temp}} > 0$ for the most dangerous mode. Unstable parallel flows are further classified as convectively unstable if initially localized pulses are amplified in at least one moving frame of reference but are damped in the laboratory frame, and absolutely unstable if such pulses lead to growing disturbances in the entire domain in the laboratory frame. To describe such an instability, we use the description of Huerre & Monkewitz (1990). An unstable parallel flow is absolutely unstable if the following criteria have all been met: (i) $\omega_{i0} := \omega_i(\alpha_0) > 0$, where α_0 is the wave number at which the complex derivative $d\omega/d\alpha$ is zero, (ii) the corresponding saddle point α_0 in the complex α -plane is the result of the coalescence of spatial branches that originate from opposite half-planes at a larger and positive value of ω_i and (iii) the saddle point pinches at ω_{i0} ; this is verified by locating a cusp at ω_{i0} in the complex ω plane (Lingwood 1997; Valluri *et al.* 2010) and ensuring that the complex wave number corresponding to the pinching point coincides with α_0 .

3.2. Ray analysis

The linear stability equations (2.7) in streamfunction form (Equation (2.10)), together with the boundary and initial conditions (2.11)–(2.12) can be neatly encoded in linear-operator form:

$$\mathcal{L}\bar{\phi} = \mathcal{M}\partial_t\bar{\phi}, \quad (3.1)$$

where we study $\bar{\phi}(x, z, t)$, the filtered streamfunction containing only positive real wave numbers (Huerre & Monkewitz 1990); here \mathcal{L} and \mathcal{M} are linear operators (cf. Equa-

tion (2.15)). When an impulsive, localized force is applied to the streamfunction, Equation (3.1) is modified:

$$\mathcal{L}\bar{\phi} + \delta(x)\delta(z)\delta(t) = \mathcal{M}\partial_t\bar{\phi}, \quad (3.2)$$

in terms of the Dirac delta function $\delta(\cdot)$. The solution of Equation (3.2) (determined here in a domain with periodic boundaries at $x = \pm L_x/2$) can be used to characterize the instability that develops from the impulse. We use the following algorithm developed by Delbende & Chomaz (1998) and Delbende *et al.* (1998), here applied to two-phase flows:

- (a) Compute the complex-valued filtered streamfunction $\bar{\phi}(x, z, t)$;
- (b) Form the L^2 -norm

$$A(x, t) = \sqrt{\int_{-\epsilon}^1 dz |\bar{\phi}(x, z, t)|^2}; \quad (3.3)$$

(c) Examine the norm along rays, $A(v, t) = A(x = vt, t)$. If $A(0, t)$ is a decreasing function of time, the instability is convective.

It suffices to consider positive and zero ray velocities only, since this enables a classification of the instability as either absolute or convective and, furthermore, in the convective case, gives information about the leading- and trailing-edge velocities of the downstream-propagating disturbance.

Additional information can be extracted from the evolution of the norm, provided the contributions to the growth of the streamfunction are dominated by a single eigenmode. This caveat does not appear in the single-phase work of Delbende & Chomaz (1998) and Delbende *et al.* (1998): those problems contain a simple means of projecting the streamfunction on to the eigenmode of interest; the spatial symmetries that produce this projection do not exist in the current problem, and this approach is therefore not applicable. We therefore assume that the evolution is dominated by a single eigenmode, and justify this assumption *a posteriori*. Thus, along rays $x = vt$, we assume that $A(x = vt, t) \sim t^{-1/2}e^{\sigma(v)t}$, where σ is the spatiotemporal growth rate of the dominant eigenmode. Therefore, we extract the finite-time estimate of the spatiotemporal growth rate as follows:

$$\sigma(v) = \frac{\ln A(vt_2, t_2) - \ln A(vt_1, t_1)}{t_2 - t_1} + \frac{1}{2} \frac{\ln t_2 - \ln t_1}{t_2 - t_1}, \quad (3.4a)$$

where t_1 and t_2 are large but finite times and $t_2 > t_1$. The complex wave number and frequency along the ray $x = vt$ also follow from this analysis (Delbende & Chomaz 1998; Delbende *et al.* 1998):

$$\alpha_i(v) = -\frac{d\sigma}{dv}, \quad (3.4b)$$

$$\omega_i(v) = \sigma(v) + \alpha_i v, \quad (3.4c)$$

$$\alpha_r(v) = \Re \left(\frac{-i \partial \bar{\phi}}{\bar{\phi} \partial x} \right)_{z=0, x=vt}, \quad (3.4d)$$

where Equation (3.4d) holds because the right-hand side is independent of time as $t \rightarrow \infty$.

3.3. Transient direct numerical simulations

Transient direct numerical simulation (DNS) of Equation (3.2) is complicated by the fact that the operator \mathcal{M} is non-invertible. To solve this equation in an optimal way, we have developed our own numerical method, which we outline here. As in Section 2, we write

$\bar{\phi}(z, t)$ as a finite sum of Chebyshev polynomials:

$$\bar{\phi}(x, z, t) = \sum_{\alpha > 0} e^{i\alpha x} \begin{cases} \sum_n a_{\alpha n} T_n \left(\frac{2z}{\epsilon} + 1 \right), & -\epsilon \leq z \leq 0, \\ \sum_n b_{\alpha n} T_n (2z - 1), & 0 \leq z \leq 1, \end{cases}$$

or more compactly,

$$\bar{\phi}(x, z, t) = \sum_{\alpha > 0} \sum_n e^{i\alpha x} v_{\alpha n} T_n(\eta_j), \quad j = L, G. \quad (3.5)$$

We substitute Equation (3.5) into Equation (3.2). This yields the following equation for the normal mode α :

$$M_\alpha \frac{d\mathbf{v}_\alpha}{dt} = L_\alpha \mathbf{v}_\alpha, \quad t > 0, \quad (3.6)$$

where M_α and L_α are the Orr–Sommerfeld matrices described in Equation (2.17). The matrix M_α is not invertible: it has rows of zeros corresponding to the no-slip boundary conditions, the continuity of the streamfunction at the interface, and the continuity of the tangential stress at the interface. Equation (3.6) is therefore a differential algebraic equation (DAE).

There are several standard methods for solving DAEs with computational software packages (Shampine *et al.* 1999). For a singular matrix M , the DAE $M(t, y)y' = f(t, y)$ has a solution only when the initial condition y_0 is consistent, that is, if there is an initial slope y_{p0} such that $M(t_0, y_0)y_{p0} = f(t_0, y_0)$. In general, computational packages for solving DAEs demand not only that the initial data be consistent, but also that the slope be prescribed as an input to the numerical solver (Shampine *et al.* 1999). We develop herein a numerical method for linear DAEs that removes the necessity to specify the slope. Moreover, long-time integrations of DAEs using computational packages can be costly, especially for the modal decomposition (3.5), which contains a large number of wave numbers. Thus, we resort to a semi-analytical solution method that holds for constant-coefficient DAEs such as Equation (3.6). We re-write Equation (3.6) as

$$\frac{d}{dt} M_\alpha \mathbf{v}_\alpha = L_\alpha \mathbf{v}_\alpha,$$

and integrate it over a numerical time step Δt :

$$M_\alpha \mathbf{v}_\alpha(t + \Delta t) - M_\alpha \mathbf{v}_\alpha(t) = \int_t^{t+\Delta t} L_\alpha \mathbf{v}_\alpha(s) ds.$$

For a sufficiently small timestep, the integral on the right-hand side may be approximated by the trapezoidal rule. Thus, the equation is approximated by

$$M_\alpha \mathbf{v}_\alpha(t + \Delta t) - M_\alpha \mathbf{v}_\alpha(t) = \frac{1}{2} \Delta t [L_\alpha \mathbf{v}_\alpha(t + \Delta t) + L_\alpha \mathbf{v}_\alpha(t)].$$

Re-arrangement gives

$$[M_\alpha - \frac{1}{2} \Delta t L_\alpha] \mathbf{v}_\alpha^{p+1} = [M_\alpha + \frac{1}{2} \Delta t L_\alpha] \mathbf{v}_\alpha^p,$$

where $\mathbf{v}_\alpha^{p+1} = \mathbf{v}_\alpha(t + \Delta t)$ and $\mathbf{v}_\alpha^p = \mathbf{v}_\alpha(t)$. The solution at an arbitrary time p is therefore available from the initial condition using only three matrix operations:

$$\mathbf{v}_\alpha^p = X_\alpha^p \mathbf{v}_{0\alpha}, \quad X_\alpha = [M_\alpha - \frac{1}{2} \Delta t L_\alpha]^{-1} [M_\alpha + \frac{1}{2} \Delta t L_\alpha]. \quad (3.7)$$

Equation (3.7) becomes an exact solution to the DAE (3.6) in the limit when $\Delta t \rightarrow 0$:

$$\mathbf{v}_\alpha(t) = \tilde{X}_\alpha(t) \mathbf{v}_{0\alpha}, \quad \tilde{X}_\alpha(t) = \lim_{\substack{\Delta t \rightarrow 0 \\ t=p\Delta t}} X_\alpha^p.$$

m	$\sigma_{\max}(\text{ST})$	$\sigma_{\max}(\text{Modal})$	$\alpha(\text{ST})$	$\alpha(\text{Modal})$
400	1.52	1.52	20	21
1300	1.39	1.39	17	17

TABLE 2. Comparison between modal and spatio-temporal analyses at various values of m , with $r = 1000$, $\epsilon = 0.1$, and $Re = 2500$. The parameters S and F are given in Equation (4.1). The DNS parameters are $N_1 = 21$, $N_2 = 60$, $L_x = 150$, $\Delta x = 0.01$, and $\Delta t = 0.01$.

Finally, to approximate a delta-function impulse, we fix the initial condition $\mathbf{v}_{0\alpha}$ as follows:

$$\bar{\phi}(x, z, t = 0) = \sum_{\alpha > 0} e^{i\alpha x} e^{-\alpha^2 w_x^2} \begin{cases} \sum_n \frac{N_n}{\sqrt{\pi w_z^2}} T_n(\eta_L) \int_{-1}^1 ds e^{-[\epsilon(s-1)/2]^2 / w_z^2} \frac{T_n(s)}{\sqrt{1-s^2}}, & z \leq 0, \\ \sum_n \frac{N_n}{\sqrt{\pi w_z^2}} T_n(\eta_G) \int_{-1}^1 ds e^{-[(s+1)/2]^2 / w_z^2} \frac{T_n(s)}{\sqrt{1-s^2}}, & z \geq 0, \end{cases}$$

where $N_n = 1/\pi$ if $n = 0$ and $2/\pi$ otherwise. The coefficients w_x and w_z are the widths of the approximate delta functions in the x - and z -directions respectively.

This solution method is appropriate for the kind of long-time simulations performed herein because the time required on a computer to implement Equation (3.7) depends only very weakly on p : the computation time required to raise an arbitrary square matrix to the p^{th} power depends (in a worst-case-scenario) only logarithmically on p (Ar & Cai 1994). Thus a DNS of 1000 time units takes (at most) only three times longer than a DNS of 10 time units.

We have validated the solution method by computing the growth rate for delocalized monochromatic initial conditions, and checking that the dispersion curve agrees with standard (temporal) eigenvalue analysis: the results are identical in each case and are not reported further here. We have further validated the spatio-temporal transient DNS by using Equations (3.4) and computing the growth rate and wave number at the most dangerous spatio-temporal mode. This is necessarily the most dangerous temporal mode (Huerre & Monkewitz 1990). Thus, if our transient DNS is correct, then the maximum growth rate computed in this manner must agree with standard temporal eigenvalue analysis. The results for this comparison are shown in Table 2, and confirm the correctness of our transient DNS. We now apply this method to classify completely the instability in turbulent two-phase stratified flow.

4. Results for the turbulent base state

4.1. Modal analysis and flow-regime maps

In this section we examine the spatio-temporal instability wherein the upper layer is turbulent. We base the parameter values on an upper layer of air of depth $d_G = 5$ cm, together with the values of surface tension and gravitational acceleration given in Table 1 (these parameter values were used in Ó Náraigh *et al.* (2011a)). Substituting these values into Equation (2.14), we obtain

$$F_0 = 3.7809 \times 10^6, \quad S_0 = 1.1420 \times 10^7. \quad (4.1)$$

Starting with the base state described in Section 2, we carry out a *modal* analysis for the turbulent case. The results are shown in Figure 2. Here, we have fixed $Re = 2350$ and $\epsilon = 0.1$, and have chosen the value of m to give a convective/absolute (C/A) transition, such that the main saddle point in the contour plot for the largest value of ω_i has just

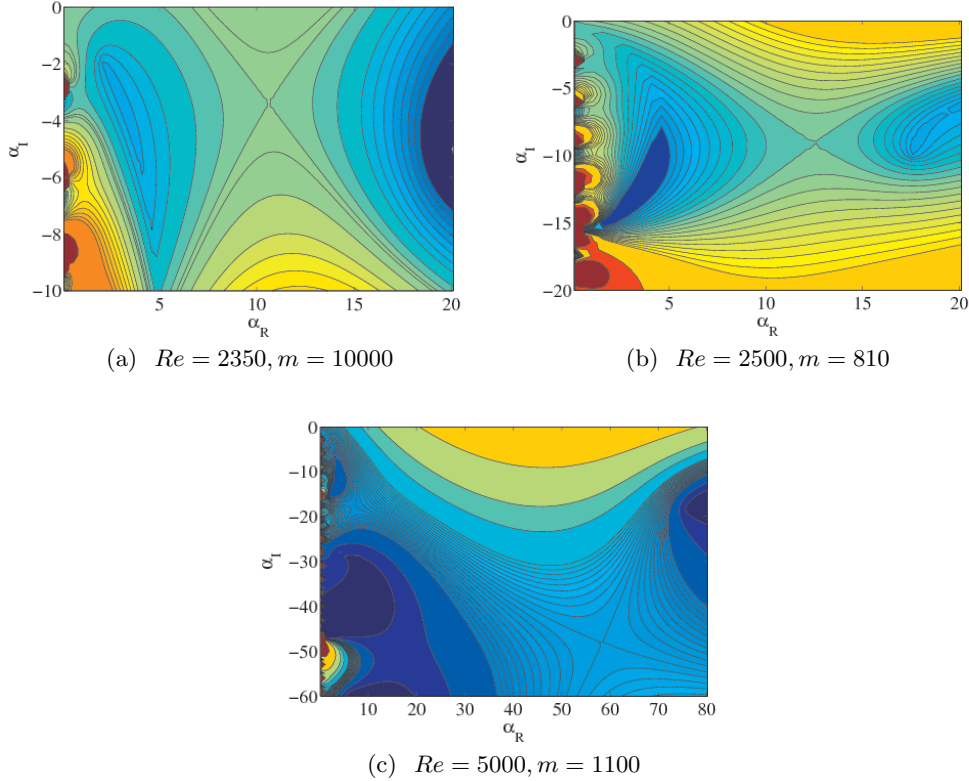


FIGURE 2. Contour plot in the complex wave number plane of the largest ω value. In all cases, $r = 1000$, $\epsilon = 0.1$, and F_0 and S_0 are given by Equation (4.1).

become positive. The other conditions described in Section 3.1 that are required for absolute instability also apply. However, from Figure 2, it is not certain that the system is indeed absolutely unstable, given the odd features near the imaginary axis caused by different eigenmodes being dominant in different parts of the complex wave number plane.

Therefore, we turn to the ray analysis, representative results from which are shown in Figure 3. The two cases are chosen for clarity, since they lie away from (and at opposite sides of) the C/A transition such that the respective convective and absolute behaviour is clearly visible. In this figure, the amplification of a pulse is very large. This poses a practical problem when trying to infer a C/A transition: when starting from an absolutely unstable case and repeating the analysis for a slightly different value of the parameter m , a convective instability is found when the left tail of the signal decreases as time goes by. But the tails of the pulse are close to the part of the x -domain that is affected by numerical error. Moreover, for large m , the strong amplification of all parts of the pulse makes a comparison of signal tails difficult. The accuracy with which a C/A transition can be determined with the ray analysis is therefore limited. That being as it may be, close inspection of the ray analysis results near the C/A transitions inferred from a modal analysis confirms the latter.

Carrying on from these studies, we have constructed a flow-regime map using the modal analysis. We have carefully followed the dominant saddle points such as those in Figure 2, and have performed the necessary checks required for confirming absolute

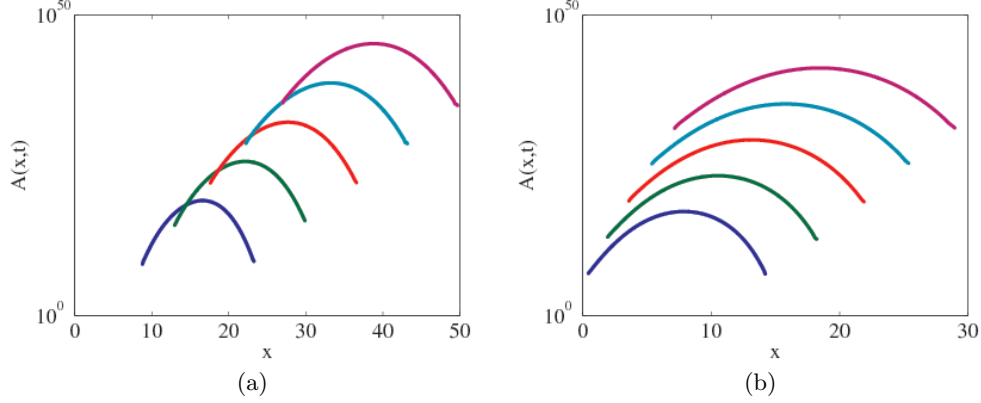


FIGURE 3. The norm $A(x,t)$ for (a) $m = 400$ (convective); (b) $m = 1300$ (absolute), at $t = 30, 40, 50, 60, 70$ (from bottom to top). The other parameters are $r = 1000$, $Re = 2500$, $\epsilon = 0.1$, and S and F are given in Equation (4.1). The DNS parameters are $N_1 = 21$, $N_2 = 60$, $L_x = 150$, $\Delta x = 0.01$, and $\Delta t = 0.01$. Only a fraction of the x domain is shown.

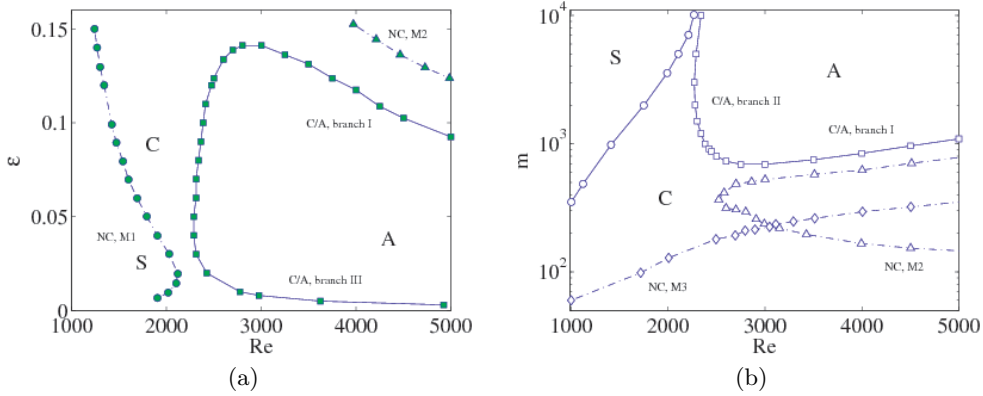


FIGURE 4. Flow-regime map for the turbulent base state. Here, $r = 1000$ and S and F , are given in Equation (4.1). Mode M1 can be stable (S, neutral curve marked with circles), convectively unstable (C), or absolutely unstable (A, C/A transition curve marked with squares). Further modes, called M2 and M3, can be convectively unstable, with neutral curves (‘NC’) given by dashed lines and labelled by triangles and diamonds respectively. (a) Variations in ϵ at fixed $m = 1000$; (b) Variations in m at fixed $\epsilon = 0.1$.

instability (Section 3.1). Our modal studies have furthermore been confirmed by the ray analysis discussed above. In Figure 4(a), we see that if Re is increased for a fixed value of m , the system generally goes from a stable state, through a convectively unstable to an absolutely unstable state. Figure 4(b) shows that the convectively unstable regime can disappear entirely, when large values of m are used. The same figure also shows that the neutral curve ‘pushes’ the C/A transition at large values of m back to higher Re -values; this is discussed further below. We note in Figure 4(b) the presence of two additional modes of instability whose neutral curves are marked ‘NC:M2’ and ‘NC:M3’; hence, three modes are convectively unstable. A standard temporal energy-budget analysis conducted at $Re = 5000$, $m = 600$, confirms that M2 and M3 both derive most of the destabilizing energy from the interfacial region, and a small contribution from the liquid layer.

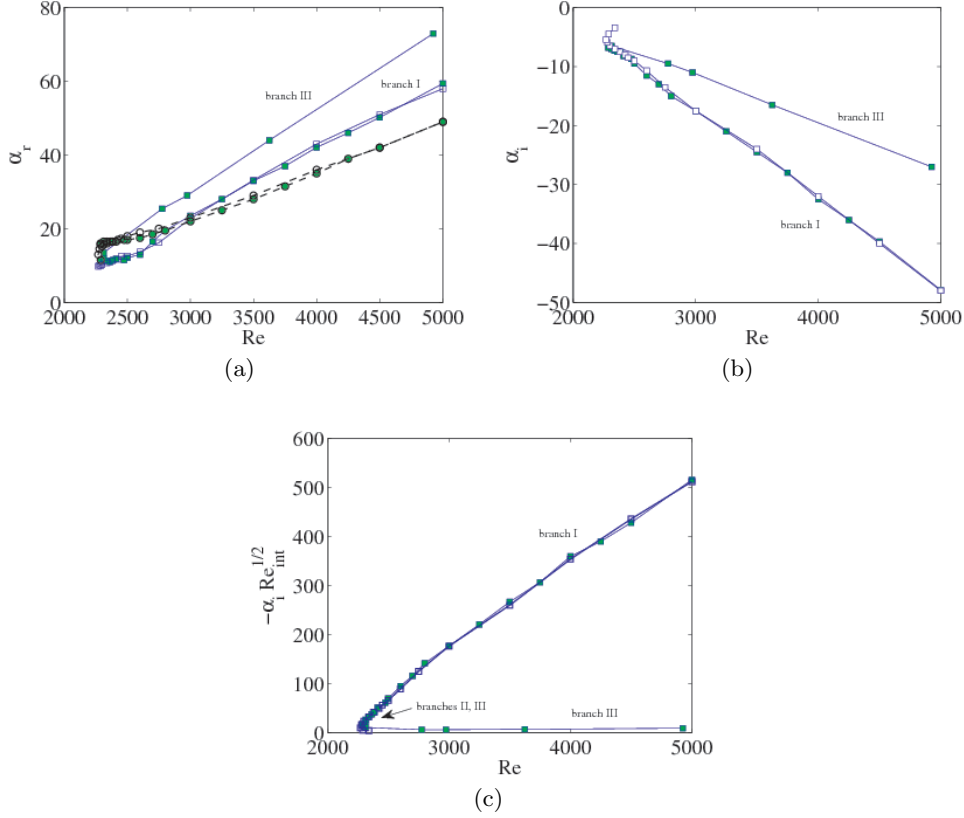


FIGURE 5. The complex wave number along the C/A transition in Figure 4 as a function of Re (squares, solid lines). In (a), the wavenumber of the most dangerous temporal mode is also shown (circles, dashed line). Filled squares: variation in ϵ at fixed m ; empty squares: variation in m at fixed ϵ . Panel (c) is a rescaled version of the imaginary wave number in (b).

The profile of the wave-induced Reynolds stress has also confirmed that they are both conventional ‘internal modes’ in the liquid (Boomkamp & Miesen 1996; Ó Náraigh *et al.* 2011a). However, these modes differ in one respect: M2 has a speed comparable to, but less than, the interfacial velocity whereas M3 is much slower, especially at large Reynolds numbers.

In Figure 5, we examine the complex wave number (α_r, α_i) at the C/A transition. We have plotted α_r as a function of Re for various (ϵ, m) combinations; we have also plotted $\alpha_i (Re_{int})^{1/2}$ in the same manner. Here $Re_{int} = rU_{int}\epsilon/m$ is the liquid Reynolds number based on the base-state velocity at the interface, U_{int} (the reason for this rescaling will become apparent in what follows). Figure 5(a,b) demonstrates that α_r at the transition is governed primarily by Re . The real and imaginary parts of the wave number both increase significantly with Re . By rescaling the wavenumbers with respect to the lower-layer depth (i.e. letting $\alpha_r \rightarrow \epsilon\alpha_r$), this variation is given some context: for $Re = 1000$ the wavelength is comparable to the liquid-layer depth, while for $Re = 5000$ it is approximately 10 times smaller than the liquid-layer depth. Figure 5(a) also indicates that α_r at the saddle point along the neutral C/A curve closely follows α_r for the most-dangerous temporal mode. This confirms the observation in Figure 2 that the saddle point lies almost directly below the most dangerous temporal mode. This is explained as follows: for all the cases

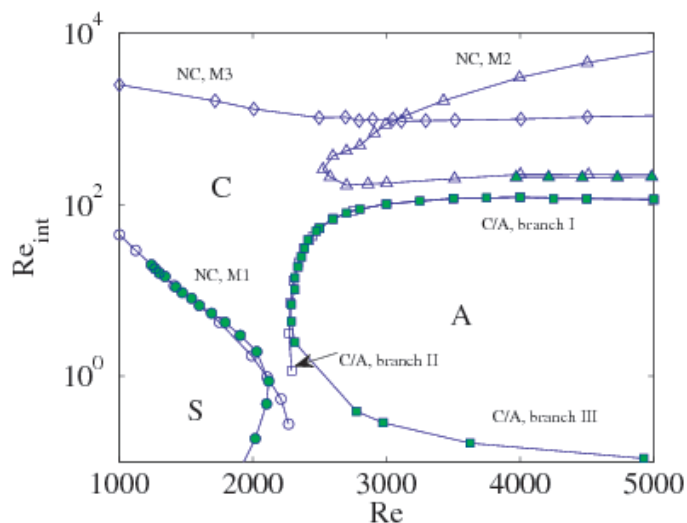


FIGURE 6. Reduced flow-regime map for the turbulent base state. Filled symbols: variation in ϵ at fixed m ; empty symbols: variation in m at fixed ϵ .

considered here, the group velocity $d\omega_r/d\alpha_r$ calculated for temporal modes depends only weakly on α_r , and a straightforward application of the Cauchy–Riemann conditions to the analytic function $\omega = \omega_r(\alpha_r, \alpha_i) + i\omega_i(\alpha_r, \alpha_i)$ shows that for such group velocities, the α_r -values for the most-dangerous temporal mode and the saddle-point mode coincide.

Most of the results in Figure 4(a,b) collapse into one plot, namely Figure 6(a). Almost all corresponding boundaries obtained for Figure 4(a,b) collapse. Especially of interest is the large- Re /large- Re_{int} behaviour of the C/A transition (branch I), which corresponds to a critical value of Re_{int} that is virtually independent of Re . It is possible to explain this scaling behaviour using the theory developed by Ó Náraigh *et al.* (2012) (see also Appendix A). There, the spatio-temporal growth rate $\omega_i(\alpha_r, \alpha_i)$ is prescribed in terms of a Taylor series in α_i , where the coefficients in the Taylor series are derived from the purely temporal linear stability analysis, and depend on α_r . We have verified that the C/A transition curves in Figure 6 are described accurately by a quadratic truncation of this Taylor series (Appendix A). In this ‘quadratic approximation’, the saddle point occurs at $\alpha_r = \alpha_r^*$, where α_r^* solves

$$\left. \frac{d\omega_i^{\text{temp}}}{d\alpha_r} \frac{d^2\omega_i^{\text{temp}}}{d\alpha_r^2} \right|_{\alpha_r^*} = -c_g(\alpha_r^*) \frac{dc_g}{d\alpha_r} \Big|_{\alpha_r^*}. \quad (4.2)$$

In the current application, the group velocity is approximately constant, hence $\alpha_r^* \approx \alpha_{r,\text{max}}$, the location of the most-dangerous temporal mode. The same quadratic approximation gives the following condition for the onset of absolute instability:

$$-\left. \frac{d^2\omega_i^{\text{temp}}}{d\alpha_r^2} \right|_{\alpha_r^*} \omega_i^{\text{temp}}(\alpha_r^*) = \frac{1}{2} c_g^2(\alpha_r^*). \quad (4.3)$$

We now approximate each term in Equation (4.3). Consider first of all the right-hand side. Previous work (Ó Náraigh *et al.* 2011a) demonstrates that the group velocity c_g is only slightly in excess of the interfacial velocity U_{int} (this is also consistent with experiments, e.g. Cohen & Hanratty (1965)). Thus, we approximate the group velocity as $c_g \approx U_{\text{int}}$. Moreover, since the liquid layer is thin and viscous, the base-state velocity

in the liquid is close to linear shear flow. In addition, for thin films, $Re_* = \theta Re$, where θ is a geometric factor independent of the flow parameters (Ó Náraigh *et al.* 2011a). Thus, we have the following string of equalities:

$$\frac{U_{\text{int}}}{U_0} \approx \frac{\tau_i d_L}{\mu_L U_0} = \frac{\epsilon}{m} \frac{Re_*^2}{Re} = \frac{\epsilon}{m} \theta^2 Re.$$

But

$$Re_{\text{int}} = \frac{\rho_L U_{\text{int}} d_L}{\mu_L} = \frac{r}{\theta^2} \left(\frac{U_{\text{int}}}{U_0} \right)^2,$$

hence

$$\frac{U_{\text{int}}}{U_0} = \left(\theta / r^{1/2} \right) Re_{\text{int}}^{1/2},$$

and

$$c_g^2 \approx (\theta^2 / r) Re_{\text{int}}. \quad (4.4)$$

Next, we consider the left-hand side. We use the quadratic approximation

$$\omega_i^{\text{temp}} = A\alpha - \frac{1}{2}B\alpha^2, \quad A, B > 0.$$

Note that this is not a long-wave approximation, but is instead a fit to the data around the most-dangerous temporal mode, where the fitting parameters A and B are selected with respect to the actual, computed values of the maximum growth rate, expressed as $\max(\omega_i^{\text{temp}}) = A^2/(2B)$, and the cutoff wave number, written as $\alpha_0 = 2A/B$. We now consider three parameter regimes and investigate the functional dependence of A and B on the Reynolds number Re .

Functional dependence for fixed $\epsilon \approx 0.1$ and varying m : At large Reynolds numbers, both the growth rate and the cutoff wave number increase linearly with Re . We write

$$\max(\omega_i^{\text{temp}}) = k_1 Re, \quad \alpha_0 = k_2 Re,$$

where k_1 and k_2 are constants of proportionality; these are measured to be m -independent (Figure 7). In other words,

$$\frac{1}{2}(A^2/B) = k_1 Re, \quad 2A/B = k_2 Re.$$

Hence, $A^2 = 2k_1 Re(2A/Re k_2)$, or $A = 4k_1/k_2$. At maximum growth,

$$-\omega_i^{\text{temp}} \frac{d^2 \omega_i^{\text{temp}}}{d\alpha_r^2} \Big|_{\alpha_r, \max} = \frac{1}{2} A^2 = 8k_1^2/k_2^2, \quad (4.5)$$

and the LHS of the C/A transition criterion is independent of Re for large values of Re . Combining Equations (4.3), (4.4), and (4.5), we have the following criterion for the onset of absolute instability:

$$Re_{\text{int}} = C_1, \quad C_1 = \frac{16rk_1^2}{k_2^2\theta^2},$$

where C_1 is a parameter-independent constant. Hence, at large Re , there is a critical Reynolds number Re_{int} for the onset of absolute instability. This is consistent with figure 6 (branch I).

On the other hand, for smaller values of Re , Figure 7 gives

$$\max(\omega_i^{\text{temp}}) \propto |Re - Re_c|^p, \quad p > 1,$$

where Re_c is approximately independent of m . We have also measured the cutoff wave

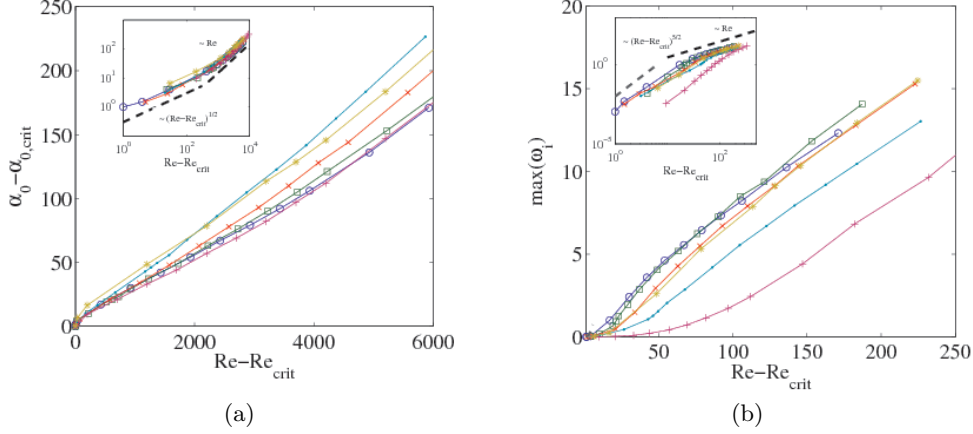


FIGURE 7. Dependence of the *temporal* problem on the system parameters. (a) The cutoff wavenumber α_0 , for which $\omega_i^{\text{temp}}(\alpha_0) = 0$; (b) the maximum growth rate $\max(\omega_i^{\text{temp}})$. The parameters to be varied are the pair (m, ϵ) . Circles: (4000,0.1), Squares: (2000,0.1), Crosses: (1000,0.1); Diamonds: (500,0.1); Dashes: (1000,0.005); Stars: (1000,0.05). Trendlines have been added to the insets.

number as

$$\alpha_0 = \alpha_{0c} + k_3 |Re - Re_c|^{1/q}, \quad q > 1,$$

where α_{0c} and k_3 are approximately independent of m . (We have found $p \approx 5/2$, $q \approx 2$; see Figure 7.) Putting these facts together, we get

$$-\omega_i^{\text{temp}} \frac{d^2 \omega_i^{\text{temp}}}{d\alpha_r^2} \Big|_{\max} \propto \frac{1}{\alpha_{0c}^2} |Re - Re_c|^{2p}, \quad Re \rightarrow Re_c,$$

and the criterion for the onset of absolute instability is therefore

$$Re_{\text{int}} = C_2 |Re - Re_c|^{2p},$$

where C_2 is independent of m . This relation is consistent with figure 6 (branch II).

Functional dependence for fixed m and varying ϵ : At large Reynolds numbers and relatively large values Re_{int} such that $\epsilon \approx 0.1$, both the growth rate and the cutoff wave number increase linearly with Re (Figure 7). Thus, the scaling arguments employed for fixed ϵ and varying m pertain here also, and the criterion for absolute instability is again $Re_{\text{int}} = C_1$, where C_1 is a parameter-free constant. This relation is again consistent with Figure 6 (branch I). For smaller values of Re , but for still relatively large values of Re_{int} , Figure 7 gives

$$\max(\omega_i^{\text{temp}}) \propto |Re - Re_c(\epsilon)|^p, \quad p > 1,$$

where $Re_c(\epsilon)$ is approximately independent of m but depends on ϵ . We have also measured the cutoff wave number as

$$\alpha_0 = \alpha_{0c}(\epsilon) + k_3 |Re - Re_c(\epsilon)|^{1/q}, \quad q > 1,$$

where $\alpha_{0c}(\epsilon)$ is approximately independent of m but dependent on ϵ , and where k_3 is independent of m and ϵ . Putting these facts together, we get

$$-\omega_i^{\text{temp}} \frac{d^2 \omega_i^{\text{temp}}}{d\alpha_r^2} \Big|_{\alpha_r, \max} \propto \frac{1}{\alpha_{0c}^2(\epsilon)} |Re - Re_c(\epsilon)|^{2p}, \quad Re \rightarrow Re_c,$$

and the criterion for the onset of absolute instability is therefore

$$Re_{\text{int}} = \frac{C_2}{\alpha_{0c}(\epsilon)} |Re - Re_c(\epsilon)|^{2p},$$

where C_1 is independent of m . This relation is consistent with Figure 6 (branch III, large Re_{int}), in the sense that the stability boundary depends on Re_{int} , Re , and ϵ .

As ϵ is reduced, the Reynolds number Re_{int} is also reduced. In such a regime, and for large values of Re , we have

$$\max(\omega_i^{\text{temp}}) = k_4 \epsilon Re^2 / m, \quad \alpha_0 = k_5 Re,$$

where k_4 and k_5 are constants of proportionality. In other words,

$$\frac{1}{2}(A^2/B) = k_4 \epsilon Re^2 / m, \quad 2A/B = k_5 Re,$$

Hence, $A = 4k_4 \epsilon Re / (k_5 m)$, and $B = 8k_4 \epsilon / (k_5 m)$. Thus, at maximum growth,

$$-\omega_i^{\text{temp}} \frac{d^2 \omega_i^{\text{temp}}}{d\alpha_r^2} \Big|_{\max} = \frac{1}{2} a^2 = \frac{8k_4^2 \epsilon^2 Re^2}{k_5^2 m^2} \propto Re_{\text{int}}^2.$$

Therefore, in this case, the LHS of the C/A transition criterion is proportional to Re_{int}^2 , while the RHS is proportional to Re_{int} . Therefore, there is a *minimum* value of Re_{int} (rather than a maximum value) for absolute instability. This corresponds precisely to the lower-branch C/A transition curve in Figure 6 (branch III, small Re_{int}).

These results have been presented for fixed values of F_0 and S_0 . We briefly sketch the effect of varying these parameters. Increasing F_0 is stabilizing, and raises the critical Reynolds number Re_c for the onset of temporal instability. This suggests that branches II and III should shift to the right under such an increase. Similarly, increasing S_0 makes the temporal disturbances more stable, the main effect of which is (counter-intuitively) to *increase* $-\omega_i^{\text{temp}} d^2 \omega_i^{\text{temp}} / d\alpha_r^2$ at $\alpha_r = \alpha_{r,\max}$, which implies that the critical Reynolds number Re_{int} for the onset of absolute instability at large Re and Re_{int} should be *raised*. We have performed some detailed calculations for the onset of absolute instability with the ‘full’ dispersion relation, the results of which agree with this description provided by the quadratic approximation.

We also comment on the scaling behaviour for the imaginary part of the wave number at the C/A transition. The value of α_i at transition in the quadratic approximation is

$$\alpha_i = -2 \max(\omega_i^{\text{temp}}) / c_g.$$

Approximating $c_g \propto \sqrt{Re_{\text{int}}}$, we have $\alpha_i \sqrt{Re_{\text{int}}} \propto -\max(\omega_i^{\text{temp}})$. For large values of the Reynolds numbers Re and Re_{int} , we have $\max(\omega_i^{\text{temp}}) \propto Re$, where the constant of proportionality is parameter-free. This gives $-\alpha_i \sqrt{Re_{\text{int}}} \propto Re$, in agreement with Figure 5.

One further result concerns the alignment of branch I (main C/A transition, Figure 6) with the neutral temporal stability curve of M2. It is as if the absolute instability is quenched when M2 becomes unstable. This is due to mode competition, which occurs in a convectively unstable regime close to the C/A boundary, in which both M1 and M2 are unstable, with a wave length comparable to the liquid-layer depth. In Figure 8, the contours of ω_r are shown for the least stable mode at each complex α . This case involves the parameter values $Re = 5000$, $\epsilon = 0.1$, and $m = 600$. The spatial curve $\omega_i = 0$ of the most dangerous mode is identified with M1 by a Gaster-type analysis (see Gaster (1962) and Appendix B). The contours $\omega_r = \text{Const.}$ that connect orthogonally to the spatial curve are identified also with M1. The orthogonality of contours of the real and

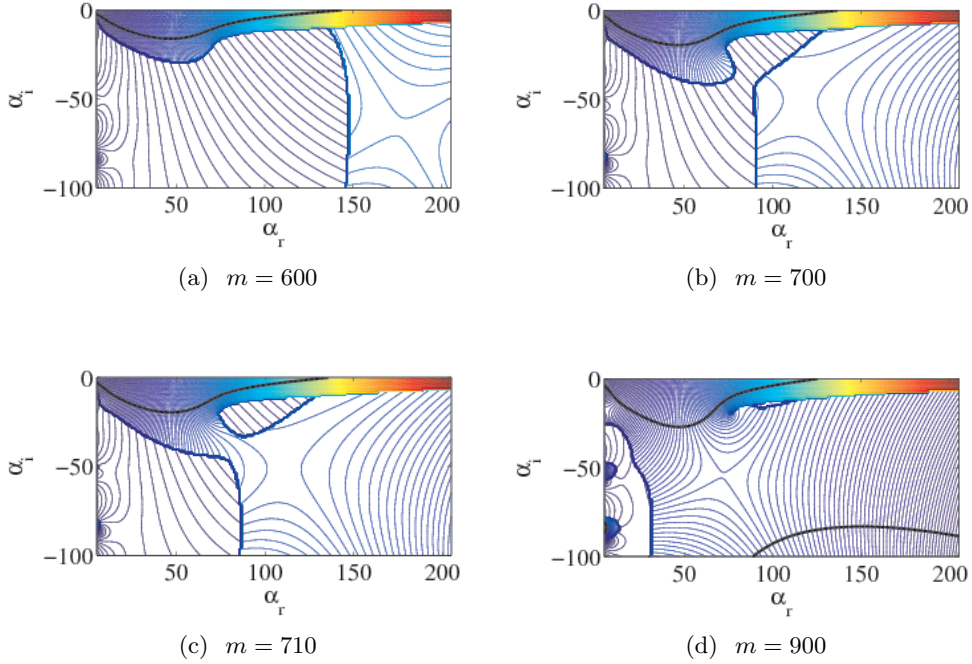


FIGURE 8. Spatio-temporal mode competition and the C/A transition: contour plots of ω_r for the most dangerous mode in the complex α -plane. The black lines represent the spatial curve $\omega_i = 0$ of M1. Here $Re = 5000$, and $\epsilon = 0.1$. The M2 temporal mode is unstable for $m < 800$, and the C/A transition occurs near $m = 1100$. The sharp jumps in ω_r represent mode competition between M1 and M2, and the saddle point in (a),(b) does not correspond to M1.

imaginary parts of an analytic function is a straightforward consequence of the Cauchy–Riemann conditions. In this way, we have established in Figure 8(a) that the saddle point (a necessary precursor for absolute instability) does not originate from the M1-eigenmode. However, upon increasing m (Figs. 8(b–d)), the region of α -space in which M1 dominates fills out, and the spatial curve of M1 connects to a saddle: it is as if the dominant saddle point ‘switches’ from non-M1 to M1. Going to higher values of m , the sign of ω_i at the saddle point becomes positive, and absolute instability ensues.

We have investigated in more depth the identity of the rival saddle points by using the quadratic approximation, which provides a direct connection between the spatio-temporal and temporal modes. By reconstructing Figure 8 from the quadratic approximation (not shown), we have confirmed the spatio-temporal mode competition. Care has been taken to ensure correct identification of the dispersion curves by double-checking the continuity in α_r of the corresponding ω_r curves. In a reconstruction of the ω_i -landscape of M1, a saddle point exists at $\alpha_r \approx \alpha_{r,\max}$. In a further reconstruction, two additional saddle points occur, and are connected with M2: one lies near $\alpha_{r,\max}$, while a further saddle point resides at large α_r . Finally, we have verified that as m increases, the values of ω_i associated with M1 increase (especially near the saddle point), eventually leading to absolute instability; the other saddles are simultaneously overwhelmed by this increase and no longer produce mode competition.

4.2. Energy budget

The purpose of applying an energy-budget analysis is to infer the mechanism for instability generation. In view of the connection between spatio-temporal and temporal modes exemplified in the quadratic approximation considered in Section 4.1, a spatio-temporal energy-budget analysis necessarily inherits the properties of the corresponding temporal analysis. Nevertheless, we consider the energy-budget analysis in this section, and investigate how such a study applies to the growth of a pulse (as opposed to a normal mode). The ray analysis provides a means of examining such pulses.

We examine the mechanism by which the pulse grows, noting that this does not have to be the same throughout the pulse. We introduce the kinetic energy density

$$K(x, t) = \frac{1}{2} \int_{-\epsilon}^0 dz r_L |\delta \mathbf{u}|^2 + \frac{1}{2} \int_0^1 dz r_G |\delta \mathbf{u}|^2, \quad (4.6)$$

where $\delta \mathbf{u} = (\delta u, \delta w)$ is the perturbation velocity. We differentiate this expression with respect to time at a fixed location x , and apply the equations of motion (2.7) and Gauss's divergence theorem to obtain the following flux-conservation equation:

$$\frac{\partial K}{\partial t} + \frac{\partial F_K}{\partial x} = s_B(x, t) + s_I(x, t), \quad (4.7)$$

where the source/sink terms s_B and s_I , and the flux F_K are described in what follows. First, we introduce the following notation for the perturbative contribution to the viscous stress tensor δT_{ij} :

$$\delta T_{ij} = -\delta_{ij} \delta p + \frac{m_j}{Re} \left(\frac{\partial}{\partial x_i} \delta u_j + \frac{\partial}{\partial x_j} \delta u_i \right);$$

we also denote the separate fluid domains by $(a_L, b_L) = (-\epsilon, 0)$ and $(a_G, b_G) = (0, d_G)$. The flux F_K can then be written as

$$F_K(x, t) = \int_{a_L}^{b_L} dz \left[\frac{1}{2} r_L U_0(z) |\delta \mathbf{u}|^2 - \delta u \delta T_{xx} - \delta w \delta T_{xz} \right] \\ + \int_{a_G}^{b_G} dz \left[\frac{1}{2} r_G U_0(z) |\delta \mathbf{u}|^2 - \delta u \delta T_{xx} - \delta w \delta T_{xz} \right].$$

In a similar manner, the bulk source/sink term takes the form

$$s_B(x, t) = \sum_{j=L, G} [REY_j(x, t) + DISS_j(x, t)], \\ REY_j(x, t) = -r_j \int_{a_j}^{b_j} dz \delta u \delta w \frac{dU_0}{dz}, \\ DISS_j(x, t) = -\frac{m_j}{Re} \int_{a_j}^{b_j} dz \left[2(\delta u_x)^2 + 2(\delta w_z)^2 + (\delta u_z + \delta w_x)^2 \right],$$

and finally, the interfacial source/sink $s_I(x, t)$ is given by

$$s_I(x, t) = TAN(x, t) + NOR(x, t), \\ TAN(x, t) = (\delta T_{zx}^L \delta u^L - \delta T_{zx}^G \delta u^G)_{z=0}, \\ NOR(x, t) = (\delta T_{zz}^L \delta w^L - \delta T_{zz}^G \delta w^G)_{z=0}.$$

There are no contributions to the energy balance from the perturbation turbulent stresses because these are neglected in the quasi-laminar approximation (see Section 2.2).

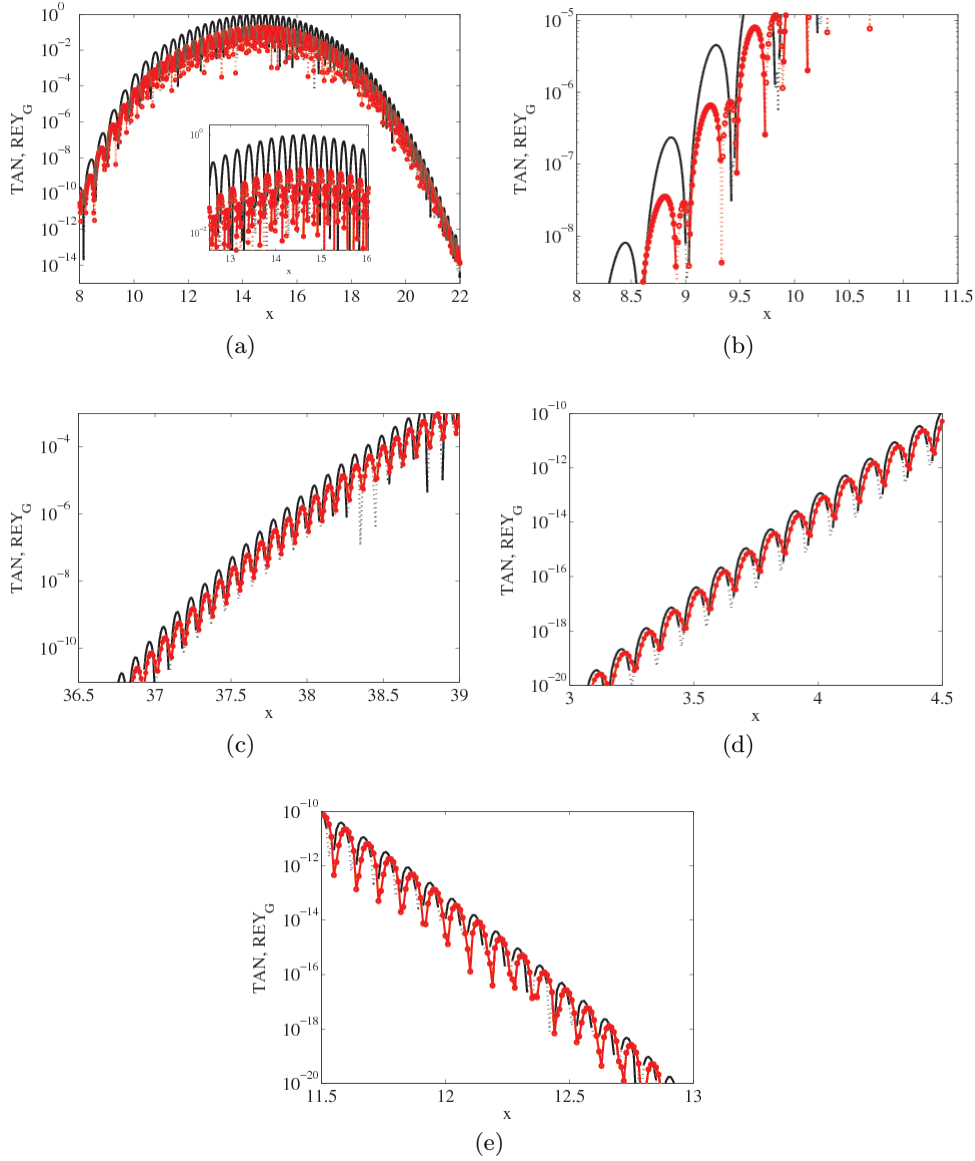


FIGURE 9. Energy budget for (a,b) $Re = 2000$, $m = 2000$ (convective); (c) $Re = 4000$, $m = 300$ (convective); (d-e), $Re = 4000$, $m = 2000$. Solid line, TAN ; Solid line with circles, REY_G ; dotted line segments represent absolute value of the same variable as along the rest of the curve. All are at $t = 50$ for $r = 1000$, $\epsilon = 0.1$.

As in previous studies of the purely temporal instability, the term TAN is identified with the viscosity-contrast instability (‘Yih mode’) (Yih 1967; Boomkamp & Miesen 1996). A positive value of this term indicates work done by the perturbations on the interface due to the viscosity jump across the interface. Again, in analogy with the purely temporal case, the term REY_L is due to an instability of Tollmien–Schlichting type in the bulk liquid flow, while positive values of REY_G correspond to an instability of the Miles type (Miles 1957) near the critical layer in the gas. Equally, the terms REY_L and

REY_G can be thought of as giving the rate at which energy is transferred from the mean flow to the disturbance via the wave-induced Reynolds stresses.

We examine these terms in detail now (the sinks $DISS_{L,G}$ are not of interest, since they are necessarily stabilising). To this end, we have selected three states (Re, m) from Figure 4(b) that intersect the near-horizontal and near-vertical parts of the C/A transition. For these states, we plot the sources and sinks as a function of x at a fixed point in time (the t -value is chosen such that all transience has been eliminated from the pulse). Naturally, the curves exhibit oscillatory behaviour (the distribution of the phase of even a single temporal mode shows oscillations). The energy budget for the purely temporal study is averaged over a single wave length, but spatial averaging is not conducted here, since the spatial distribution is the focus of the study. Therefore, we examine in Figure 9(a) a snapshot of the spatial distribution of the largest terms in the budget for $Re = 2000$, $m = 2000$, $\epsilon = 0.1$. This parameter set is seen in Figure 4(b) to be convectively unstable and to lie to the left of the C/A critical curve. The term TAN dominates throughout the pulse, followed by REY_G (other, smaller terms are not shown). For $Re = 4000$, $m = 300$, $\epsilon = 0.1$, this is also the case but, although TAN reaches locally the largest values over a wave length, its sign changes, whereas REY_G is positive virtually throughout the pulse (a zoomed view is shown in Figure 9(c)). Finally, crossing the C/A boundary (Figure 9(d-e)) causes the distribution of REY_G to become asymmetric, while the features regarding the signs of TAN and REY_G previously observed for $m = 300$ still hold.

Having characterized the turbulent base state in detail, we revisit the laminar problem and investigate whether large- r absolute instability is possible there.

5. Revisiting the laminar problem

In this section we review the problem of interfacial instability where the upper layer is laminar. Although the main conclusions for the turbulent case carry over here, some differences arise. The base-state flow $U_0(z)$ is determined in a standard fashion by solving the momentum balance

$$\mu_j \frac{d^2 U_0}{dz^2} - \frac{dP}{dL} = 0, \quad j = L, G,$$

and is subject to continuity of velocity and shear stress across the interface at $z = 0$. To facilitate comparison with previous work on laminar flows, for this section only, we adopt the non-dimensionalization scheme of Valluri *et al.* (2010). We set $\epsilon = d_L/(d_L + d_G)$ and $Re = \rho_G V (d_L + d_G)/\mu_G$, where the characteristic velocity V is chosen to be the superficial velocity $(d_L + d_G)^{-1} \int_{-d_L}^{d_G} U_0(z) dz$. The gravity and surface tension are parameterized as $\mathcal{G} := (\rho_L - \rho_G)g(d_L + d_G)^2/(\mu_G V)$ and $\mathcal{S} := \gamma/(\mu_G V)$ respectively; the value of these parameters is varied in the following parameter studies.

Because the model for the turbulent case relies on the quasi-laminar theory for the Orr–Sommerfeld perturbation equations, the streamfunction equations and the transient-DNS numerical method carry over directly to the laminar case, once the necessary rescaling and non-dimensionalization have been performed (e.g., using \mathcal{G} and \mathcal{S} in the normal stress condition).

5.1. Parametric study (1): \mathcal{G} and \mathcal{S} taken as constant

We set $\mathcal{G} = 0$ and take $\mathcal{S} = 0.01$, corresponding exactly to the paper of Valluri *et al.* (2010); this choice enables us to relate the current investigation to the results of Valluri *et al.* (2010) for liquid/liquid systems. For these parameter values, the ray analysis has

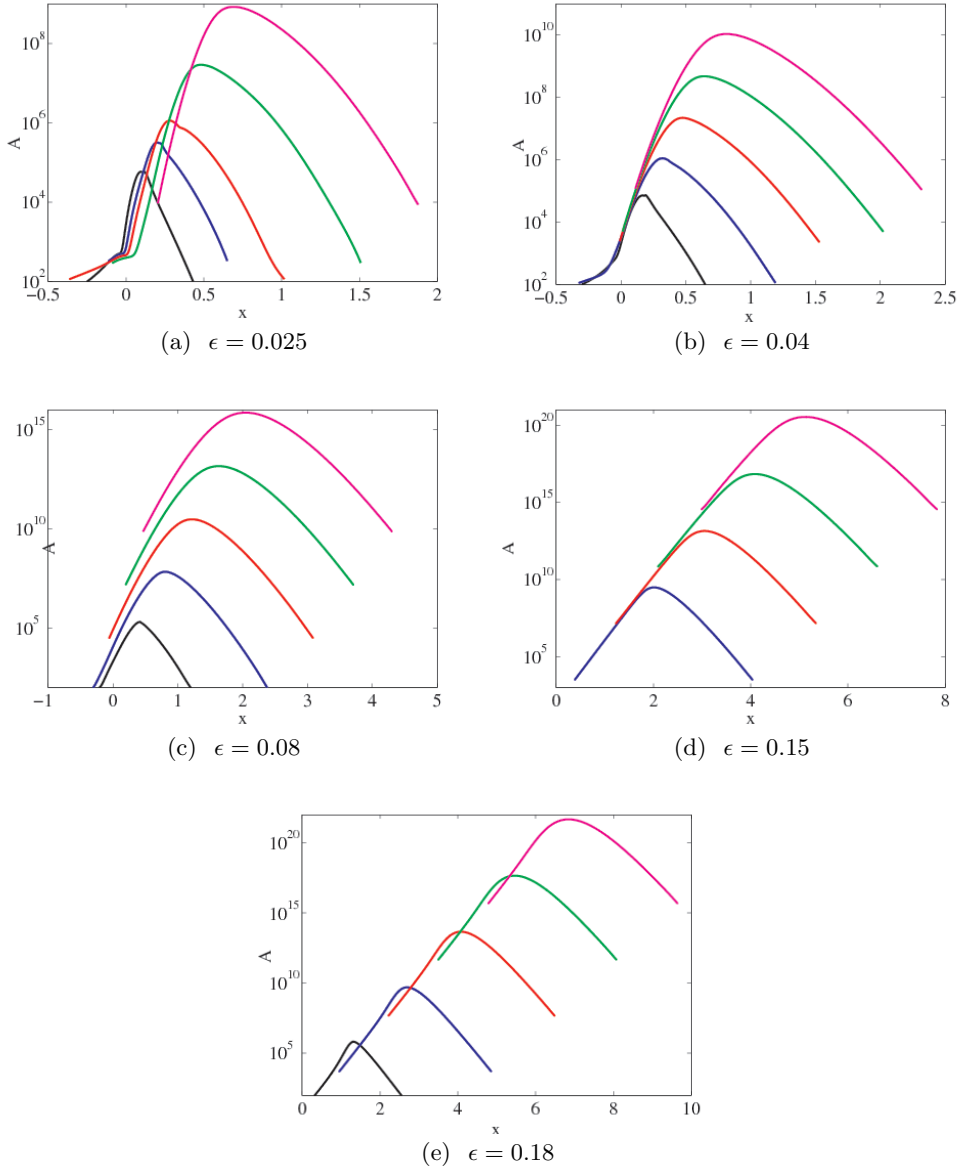


FIGURE 10. Snapshots of the norm $A(x, t)$ for different values the depth of ϵ for the laminar base state. The parameters are $Re = 1500$, $m = 150$, $r = 1000$, $S = 0.01$, and $G = 0$. (a) $t = 100, 200, 300, 500, 700$; (b)–(d) $t = 100, 200, 300, 400, 500$; (e) $t = 50, 100, 150, 200, 250$. Figures (a) and (e) are convectively unstable cases; (b)–(d) are absolutely unstable. In all cases, $L_x = 30$, $N_1 = 21$, $N_2 = 51$, the timestep is $\Delta t = 0.1$, and the grid size Δx in the x -direction is 0.003.

revealed that the laminar base state is absolutely unstable for a significant portion of parameter space, even for a density ratio of $r = 1000$. This is seen in Figure 10, where the L^2 -norm $A(x, t)$ associated with the broadband disturbance is shown at several times. These curves have been truncated at the points where they decrease below a specified fraction of their maximum value, as the finite working precision makes the results too

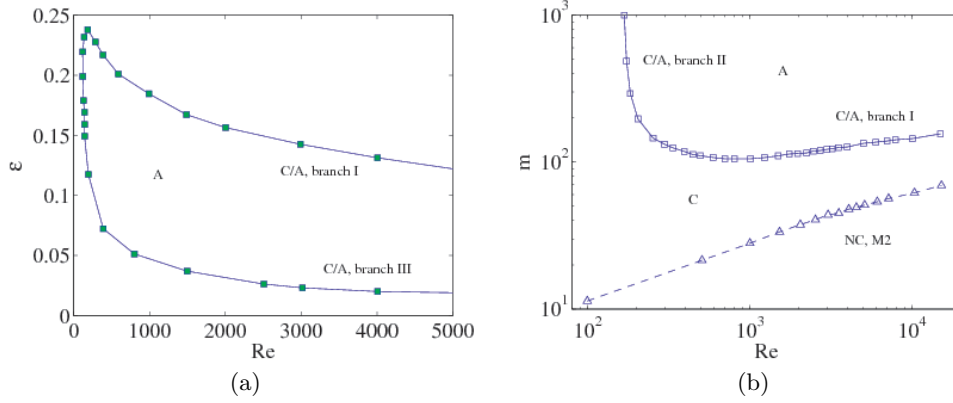


FIGURE 11. Flow-regime map showing laminar base state in parametric study (1). Here, $r = 1000$, $\mathcal{S} = 0.01$, and $\mathcal{G} = 0$. The system is always either convectively (C) unstable or absolutely (A) unstable. A second temporal mode is also unstable below the neutral curve (dashed curve labelled ‘M2’, with triangles). (a) Variations in ϵ at fixed $m = 150$; (b) Variations in m at fixed thickness $\epsilon = 0.1$.

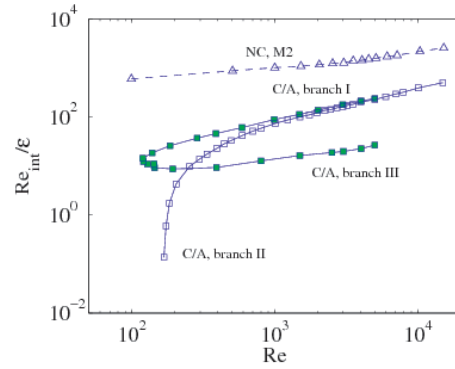


FIGURE 12. Flow-regime map of parametric study (1) in terms of the liquid Reynolds number Re_{int} . Filled symbols: variations in ϵ at constant $m = 150$; open symbols: variations in m at fixed $\epsilon = 0.1$. As described in the text, a further mode (convectively unstable) exists for $Re \gtrsim 8000$, whose neutral curve is unaffected by changes in Re_{int} , m , and ϵ .

uncertain far away from the pulse. The existence of absolute instability at large density ratios was not found in the modal analysis of Valluri *et al.* (2010), who only ascertained that density-matched fluids can become absolutely unstable. The cause for this oversight is that the magnitude of the wave number at the saddle point is very large, beyond the range searched by Valluri *et al.* (2010).

Motivated by the plots in Figure 10 showing absolute instability, we revisit the otherwise more accurate modal analysis and perform a large scan through the complex α -plane to obtain the C/A boundaries. These boundaries are consistent with the results of the ray analysis shown in Figure 10. Also, the results are similar to those in Valluri *et al.* (2010) for $r = 1$, suggesting that the transition found by Valluri *et al.* (2010) extends to density ratios of at least $r = 1000$. We have verified that, upon lowering the density ratio at a point in the absolute regime of Figure 11, also identified as such in Valluri *et al.* (2010), the system remains absolutely unstable at intermediate values of r . In contrast

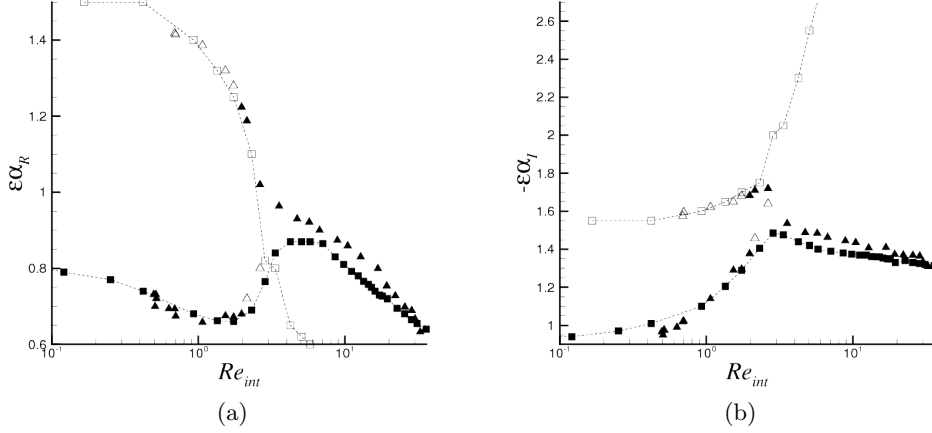


FIGURE 13. The real (a) and imaginary (b) component of the wave number at the saddle point along all C/A transitions in Figure 11(a) (squares) and Figure 11(b) (triangles), as functions of Re_{int} . The open symbols represent secondary saddle points that do not correspond to absolute instability.

to the $r = 1$ case in Valluri *et al.* (2010), for $r = 1000$, absolute instability occurs only at large m -values.

As in the turbulent case, we have examined the flow-regime boundaries in the (Re, Re_{int}) plane, where $Re_{\text{int}} := r\epsilon Re U_{\text{int}}/m$ is a Reynolds number based on the liquid-film properties and the interfacial velocity U_{int} of the base state. In contrast to the turbulent case, the results of Figure 11 do not collapse, although the overall trends otherwise bear some resemblance to the turbulent case (e.g. Figure 4): branch III corresponds to a critical value of Re_{int} (consistent with Valluri *et al.* (2010) for $r = 1$), while branch II corresponds to a critical value of Re . These two branches shift when changing the value of m , respectively ϵ , thereby contracting or expanding the absolutely unstable regime. Instead, we plot the regime boundaries in the $(Re, Re_{\text{int}}/\epsilon)$ plane in Figure 12. Although the two branches labelled ‘II’ virtually coincide in this plane (this is discussed further below), the functional form $Re_{\text{int}} = \epsilon f(Re)$ of the neutral curve differs substantially from that already encountered in the turbulent study.

We also investigate variations in the wave number at the saddle point (taken at the onset of absolute instability) in Figure 13, where $\epsilon(\alpha_r, \alpha_i)$ is plotted as a function of Re_{int} . The contrast between these results and the earlier turbulent results is remarkable. The wave number is $O(1/\epsilon)$. While the flow-regime map does not collapse in (Re, Re_{int}) -space, the wave numbers $\epsilon(\alpha_r, \alpha_i)$ depend mainly on Re_{int} , and not separately on Re . The wave number α_0 at the saddle point follows from $(d\omega/d\alpha)_{\alpha_0} = 0$, which therefore only involves a relatively simple scaling, whereas the flow regime is determined by $\omega_i(\alpha_0) > 0$, which involves more parameters. Nevertheless, the dependency of $\epsilon\alpha$ on Re_{int} is complex. Above $Re_{\text{int}} \approx 5$ (corresponding to branch I) the curves nearly collapse; a small difference remains, as is also seen in the corresponding conditions C/A transition curves in Figure 12. Upon decreasing the value of Re_{int} , two saddle points emerge. However, only one of the saddle points produces absolute instability. Most of the results in Figure 13 lie on the branch that corresponds to somewhat longer waves (note, the data represented by the filled triangles in Figure 13(a) jump from the upper to the lower branch when Re_{int}

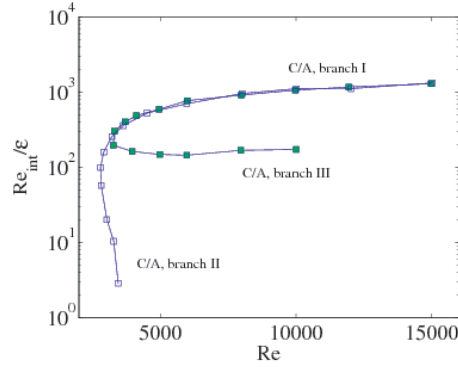


FIGURE 14. Flow-regime map for parametric study (2). Filled symbols: variations in ϵ at constant $m = 100$; open symbols: variations in m at fixed $\epsilon = 0.1$.

is decreased). These substantial differences between the turbulent and the laminar cases are now addressed in a further parametric study.

5.2. Parametric study (2): \mathcal{G} and \mathcal{S} vary inversely with Reynolds number

We extend parametric study (1) to allow for effects of gravity and surface tension corresponding to systems with a large density ratio, and we set $\mathcal{G} = \mathcal{G}_0(r - 1)/Re$ and $\mathcal{S} = \mathcal{S}_0/Re$. This extension is more reflective of real systems because it corresponds to a fixed value of the dimensional surface tension γ , while allowing for variations in \mathcal{S} through changes in the Reynolds number. Here, the values of \mathcal{G}_0 and \mathcal{S}_0 are the same as F_0 and S_0 (Section 4) but such that these are for channels that are ten times smaller: $\mathcal{G}_0 = F_0/10^3$ and $\mathcal{S}_0 = S_0/10$ unless indicated otherwise (the effect of changing these values is discussed below). The results of this parameter modification are shown in Figure 14. A striking feature of this study is the blurring of the previously sharp distinction between the turbulent case (Figure 6), and the laminar study (Figure 12). Moreover, increasing \mathcal{G} and \mathcal{S} leads to a substantial modification of the absolute region in parameter space. The role played by \mathcal{G} and \mathcal{S} in this modification is further highlighted in Tables 3–4. Table 3 corresponds to branch I, and demonstrates that an increase in \mathcal{G} or \mathcal{S} at fixed m and ϵ calls for an increase in Re to sustain absolute instability. Similarly, Table 4 corresponds to branch II, and demonstrates that an increase in \mathcal{G} at fixed Re and ϵ requires a corresponding, destabilizing increase in m to sustain absolute instability. This produces a proportional decrease in Re_{int} . The situation concerning increases in \mathcal{S} is somewhat counter-intuitive (increases in \mathcal{S} produce decreases in the critical value of m , which produce increases in the critical value of Re_{int}). However, this agrees with the turbulent case, which has already been explained using the quadratic approximation.

The scaling of the transition curves in Figure 14 can again be elucidated with the quadratic approximation. For example, for large Re and Re_{int} , we have measured

$$\max(\omega_i^{\text{temp}}) \propto (\epsilon/m^{1/2})Re^{1/4}, \quad \alpha_0 - \alpha_{0c} \propto (\epsilon^{1/2}/m^{1/2})Re^{3/4}, \quad c_g \approx U_{\text{int}} \propto \epsilon/m. \quad (5.1)$$

Plugging these scaling rules into the quadratic approximation gives $\epsilon Re/m^2 = \text{const.}$, or $Re_{\text{int}}/\epsilon = \text{const.}$ at large Re and Re_{int} , which implies the existence of a critical value of Re_{int}/ϵ along branch I. The dramatic distinction between these scaling rules and those encountered in the turbulent case owes not to some deep distinction between the respective base states, but rather arises from the distinct non-dimensionalization schemes chosen in each case. Indeed, as a final test, we have verified that a laminar

$\mathcal{G}_0/\mathcal{G}_{0,\text{ref}}$	$\mathcal{S}_0/\mathcal{S}_{0,\text{ref}}$	Re	Re_{int}	α
0.1	1	2050	0.17	$1.8 - 0.65i$
1	1	3450	0.28	$2.2 - 0.9i$
100	1	9250	0.76	$3.2 - 1.8i$
1	0.1	2750	0.23	$4.1 - 2i$
1	1	3450	0.28	$2.2 - 0.9i$
1	100	5350	0.76	$1.2 - 0.45i$

TABLE 3. Dependence of the critical parameters on surface tension and gravity at low Re_{int} (branch I, $m = 1000$, $\epsilon = 0.1$). The wavenumber at the saddle point is also stated. The uncertainty in Re is ± 50 , which also introduces an uncertainty in the values of Re_{int} and α . The symbols $\mathcal{G}_{0,\text{ref}}$ and $\mathcal{S}_{0,\text{ref}}$ refer to the reference values discussed at the beginning of the section.

$\mathcal{G}_0/\mathcal{G}_{0,\text{ref}}$	$\mathcal{S}_0/\mathcal{S}_{0,\text{ref}}$	m	Re_{int}	α
0.1	1	82.5	120	$4.1 - 3.1i$
1	1	87.5	107	$4 - 3.2i$
100	1	167.5	29	$4.1 - 3.1i$
1	0.1	122.5	55	$8.5 - 9.5i$
1	1	87.5	107	$4 - 3.2i$
1	100	77.5	136	$1.6 - 1.1i$

TABLE 4. Dependence of the critical parameters on surface tension and gravity at low Re (branch II, $Re = 10^4$, $\epsilon = 0.1$). The wavenumber at the saddle point is also stated. The uncertainty in m is ± 2.5 , which also introduces an uncertainty in the values of Re_{int} and α .

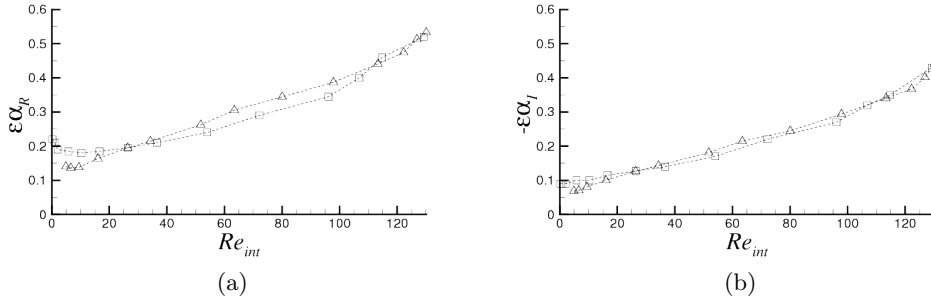


FIGURE 15. The real (a) and imaginary (b) component of the wave number at the saddle point along all C/A transitions in Figure 11(a) (squares) and Figure 11(b) (triangles), as functions of Re_{int} . The open symbols represent secondary saddle points that do not correspond to absolute instability.

temporal study, based on the non-dimensionalization scheme previously applied in the turbulent case, yields the scaling rules described in Section 4.1 (not shown).

In Figure 15 we examine again the wave number $\epsilon(\alpha_r, \alpha_i)$ at the saddle point, at the inception of absolute instability. The contrast between this figure and parametric study (1) is remarkable. In Figure 15, the results resemble those for turbulence, with one significant difference: the saddle-point mode corresponds to a much longer wave. The reason for the contrast between parametric studies (1) and (2) is due to the fact that the wave length is controlled mostly by surface tension (as demonstrated by Table 4); the surface tension in study (2) greatly exceeds that in study (1), consequently, the most unstable wave length is longer.

Referring to parametric study (1) and figure 11(b), branch II (varying m) of the C/A

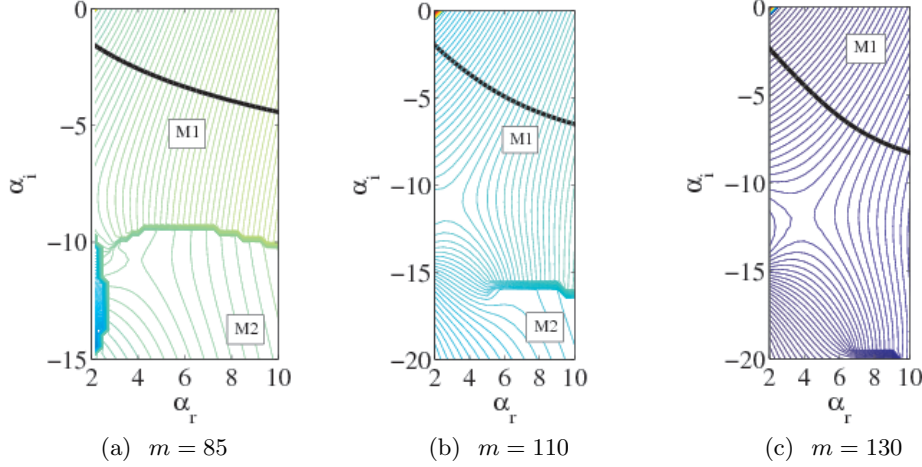


FIGURE 16. Competition between spatio-temporal modes for the laminar case. Shown are contour plots of ω_r for the most dangerous mode in the complex α plane at $Re = 20000$, $\epsilon = 0.1$ for different values of m . The black lines represent the spatial curve $\omega_i = 0$ of M1. The sharp jumps in ω_r represent mode competition between M1 and M2. The M2 temporal mode is unstable for $m < 75$, and the C/A transition occurs near $m = 170$.

transition ‘follows’ closely the neutral stability curve for a second temporal mode, M2. The same neutral curve is also present in parametric study (2), but is further removed from the C/A transition curve, and occurs at $Re_{\text{int}}/\epsilon \approx 1.5 \times 10^4$. As in the turbulent case, it is as if the existence of the M2 mode quenches the M1 absolute instability. Again, as in the turbulent case, there is clear evidence of competition between spatio-temporal modes, in addition to temporal mode competition. In Figure 16, ω_r is shown for the least stable mode at each complex α . Results are presented at different values of m for $Re = 20000$, $\epsilon = 0.1$, and $r = 1000$. The value $m = 85$ describes a situation where M2 has just become stable while M1 is convectively unstable (the point of neutral stability for M2 is at $m = 75$). The C/A transition for M1 occurs at $m = 170$. The spatial curve $\omega_i = 0$ of the most dangerous mode is identified with M1 by a Gaster-type analysis (Gaster 1962). The contours $\omega_r = \text{Const.}$ that connect orthogonally to the spatial curve are identified also with M1. In this way, we have established that the saddle point in figure 16(a) does not correspond to M1. Thus mode competition interferes most dramatically with the saddle point near the point of neutral temporal stability of M2 (near $m = 75$), while an approach to the C/A transition from within the convective regime (i.e., an increase in m from a low value) causes the mode competition to disappear gradually, thus producing a conventional single-mode saddle point. This strongly suggests that the proximity of the M2 neutral curve and the M1 C/A transition in the flow diagram is no coincidence, and is in agreement with the earlier results for the turbulent case. The same phenomenon persists for lower Reynolds numbers (e.g. $Re = 5000$). However, we have presented the results for $Re = 20000$ because this regime exhibits the mode competition most clearly. At such high Reynolds numbers, a third unstable mode comes into existence (visible in Fig. 16 in the neighbourhood $\alpha_i = 0$ and $\alpha_r = 2$). This mode has a critical Reynolds number $Re \approx 8000$ and its neutral curve is almost independent of Re_{int} , m , and ϵ . However, this third mode does not play any role in the spatio-temporal mode competition and is not discussed any further.

Finally, we have applied the spatio-temporal energy budget to the laminar flow for the

ϵ	$\sigma_{\max}(\text{ST})$	$\lambda_{\max}(\text{Modal})$	$\alpha(\text{ST})$	$\alpha(\text{Modal})$
0.18	0.0934	0.0936	15.2	16.3
0.15	0.0865	0.0866	16.9	16.5
0.12	0.0787	0.0788	17.6	17.2
0.08	0.0633	0.0633	–	20.8
0.04	0.0326	0.0326	–	30.9
0.025	0.0179	0.0179	–	43.3

TABLE 5. Comparison between modal and spatio-temporal analyses at various values of ϵ , at $r = 1000$, $m = 150$, and $Re = 1500$. The rest of the parameters are the same as in Figure 10.

cases corresponding to Figure 10(a), (c) and (e). The results indicate that over most of the pulse width, TAN dominates: this represents a source of energy for the instability that is associated with the viscosity-contrast mechanism, which dominates in temporal instability. However, REY_G also plays a significant role. In all three cases, REY_G is negative on the downstream side of the pulse, but positive on the upstream side. This is most visible in the absolutely unstable case. In contrast, for the turbulent base state, it is *only* in the absolutely unstable case that REY_G develops this asymmetry, where it even becomes the dominant term on the upstream side in the energy-budget analysis.

5.3. Ray analysis revisited

Some further information about the absolute instability of M1 is obtained from a ray analysis (Figure 17). The parameters are taken from the cases studied in Figure 10. The branches of the C/A boundary in Figure 11(a) can be mapped on to families of $\sigma(v)$ -curves in Figure 17: decreasing ϵ from $\epsilon \approx 0.18$ in the latter gives a family of $\sigma(v)$ -curves that is associated with the upper branch I of the C/A transition in Figure 11(a) (m constant, ϵ varying). As ϵ is decreased, the $\sigma(v)$ -curves shift downwards in their entirety, until the growth rate $\sigma(v = 0)$ eventually becomes positive, indicating a switchover to absolute instability. Conversely, increasing ϵ from $\epsilon \approx 0.025$ gives a family of $\sigma(v)$ -curves that is associated with the lower branch III in Figure 11(a). These curves are steep for small ϵ -values, such that $\sigma(v)$ is negative. As ϵ increases, the slope diminishes, until $\sigma(v = 0)$ is positive, and absolute instability is attained from below. Furthermore, in a convectively unstable regime at large ϵ -values, $\sigma(v)$ is linear in v for small v , and the corresponding α_r - and ω_i -values approximate negative constants, consistent with Equations (3.4). Again with reference to Equations (3.4), the upper branch in Figure 11(a) corresponds to a shift in the value v for which $\sigma = \sigma_{\max}$ (hence $\alpha_i = 0$), whereas the transition at the lower branch is associated with an increase in temporal relative to spatial growth. Finally, for large values of ϵ , the $\sigma(v)$ -curve is very wide, indicating a rapid spreading of an initial pulse, whereas for low values the pulse remains more localized.

For the cases considered herein, we have verified that the wavenumber of the spatio-temporally most dangerous mode coincides with that of the temporally most dangerous mode (Table 5). It was not possible to compute this wavenumber for all of the ϵ -values, and our finite-difference discretization of Equation (3.4d) is not always accurate. It is for this reason that we did not include α_r - v plots in Figure 17. Nevertheless, Figure 17 still contains important information: a previous set of purely spatial and purely temporal analyses (see Valluri *et al.* (2010) and Appendix B) found extremely large purely spatial growth rates (exceeding the least-negative purely spatial growth rate by an order of magnitude) that were not excited in a DNS. From the spatial growth rates along rays

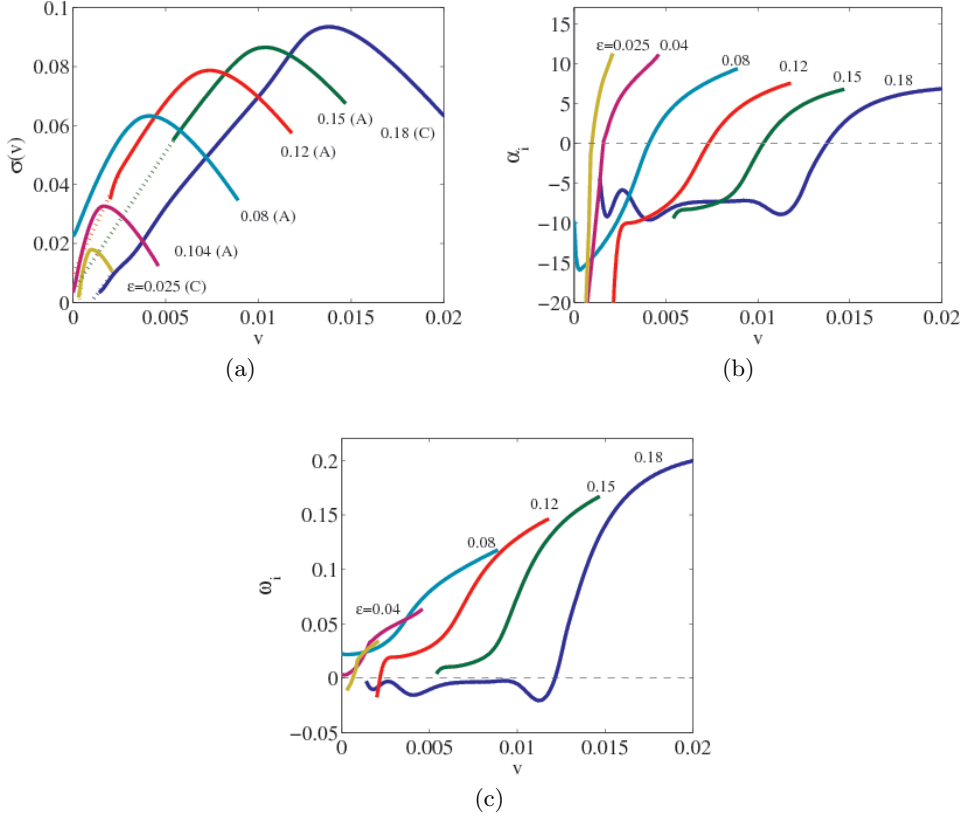


FIGURE 17. Ray analysis: (a) spatio-temporal growth rates, (b) spatial growth rates along rays; (c) temporal growth rates along rays, for laminar flow at various values of ϵ , at $r = 1000$, $m = 150$, $Re = 1500$. The rest of the parameters are the same as in Figure 10. Trend lines have been added in (a) merely to guide the eye.

in Figure 17(b), we see that such extremely large spatial growth rates are not selected, instead, the spatial growth rate comes from the same eigenmode as the temporally most dangerous mode.

6. Discussion

6.1. Flow-regime maps

It is of interest to compare our regime boundaries (e.g., Figure 6) with flow-regime maps determined from experiments. Our theory is of course applicable to water/air systems, for which channel-flow experimental studies are available. However, the results in Sec. 4 prove that water/air systems are usually convectively unstable, while the main focus of the present paper is on absolutely unstable systems. Consequently, we have searched the literature for experiments concerning air and oil, for which the viscosity contrast is much higher, and for which absolute instability is expected. We have found that such experiments were conducted on pipes (with the exception of the work by Gondret *et al.* (1999) on Hele-Shaw cells). Nevertheless, a comparison between our channel-flow model and a pipe-flow experiment is justified, since a 2D analysis may be representative of the mid-plane in pipe flow, especially for thin films, linear transverse waves (in the third

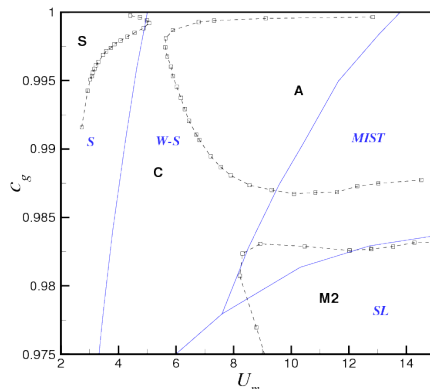


FIGURE 18. Flow-regime map Figure 4 in terms of superficial gas and liquid velocities. The curves with symbols are the present work; other solid lines and classifications in italics are experimental findings by Hoogendoorn (1959) for spindle oil/air flow in a 91mm diameter horizontal pipe wherein the following flow regimes are identified: stratified flow with a flat interface (S), wavy-stratified flow (W-S), wavy-stratified flow with suspended droplets (MIST), and slug flow (SL).

dimension) are usually overwhelmed by 2D waves, and in any case it is necessary to demonstrate that the boundaries determined in our study are not restricted to an obscure limit.

The results of Figure 4(a) are therefore presented in Figure 18 in terms of superficial velocities U_G and U_L , where $c_g = U_G/(U_G + U_L)$ and $U_m = U_G + U_L$ is the mixture velocity for parameter values approximately corresponding to the flow of air and spindle oil through a pipe of 91mm diameter, and flow-regime boundaries determined experimentally by Hoogendoorn (1959) are superposed (our data are for $m = 1000$, $r = 1000$ and the choice of S and F mentioned at the start of Section 4, which are also representative of the experimental conditions stated in Hoogendoorn (1959)). The more widely used flow-regime map by Mandane *et al.* (1974) cannot be used here, as it is for water/air systems, but they observed good agreement with water/air data also published by Hoogendoorn (1959).

We first note from Figure 18 that the neutral stability curve from the temporal analysis agrees reasonably well with the experimental data on the transition from stratified flow (i.e., no waves) to wavy stratified flow. This is expected based on the comparisons with experiments in our previous work on temporal instability, Ó Náraigh *et al.* (2011a). We note here that the superficial velocities in a 2D system are expected to be larger than for a pipe flow at the same maximal velocities in a fluid, which may have reduced the difference between the results somewhat. On the other hand, the fact that the liquid layer at the centre of the pipe is expected to be smaller due to gas pushing the liquid to the side of the pipe is expected to be of less significance, as the liquid height is the parameter along the theoretical data in the figure.

The main C/A transition is predicted theoretically here at a total superficial velocity somewhat below the experimentally determined transition from wavy-stratified flow to mist flow (waves with droplets). A relation with the onset of atomization for very viscous liquids cannot be ruled out. In fact the experimental mist flow regime lies almost entirely in the absolutely unstable regime, since the critical value of the parameter c_g for this regime is close to the high- Re C/A transition from the theory (and even more so, the M2

neutral curve). In the experiments, slug flow is observed at c_g below this critical value at large U_m . Hence slug flow is observed experimentally when according to the 2D theory the flow is convectively unstable.

6.2. Potential use in global and non-linear analyses

Although we have identified and classified the nature of the linear instability for our stated two-phase stratified problem, we briefly outline extensions that follow naturally from the present work.

The stability analysis considered throughout this paper is a ‘local analysis’ in the sense that the base flow varies on a length scale which is long relative to the wave length of the instability waves (this being true whether the analysis is linear or not). A more general approach is global stability analysis, wherein the whole of the physical domain is considered (Huerre & Monkewitz 1990; Chomaz 2005). Under such a technique, spatial streamwise variation is accounted for in both the base flow and the perturbation terms, permitting the study of nonparallel flows, i.e., no restrictions are placed on spatial scalings. Of course, such studies require appropriate computational power and therefore have only been pursued recently. In the context of the present work, such an approach permits changes in the thickness of the liquid layer which is important for many of the stated applications, but it means that ray analysis in the form used herein can no longer be employed, as periodic boundary conditions no longer apply.

The theoretical analysis required to elucidate non-linear effects discussed herein is elaborate. Thus, an important additional step might involve a numerical (e.g., DNS) study and experiments, with the aim of identifying which key non-linear effects dominate. Specifically, whether a transition to absolute instability in the nonlinear regime may precede the linear C/A transition (this has been observed by Gondret *et al.* (1999) in Hele-Shaw cells). Another question that a full numerical simulation might address concerns the location of the dominant non-linear interactions, i.e., at the phase interface or in the bulk of the liquid layer. A full numerical simulation would also permit a comparison between periodic boundary conditions (as used in the present work), and inlet conditions (as in a true channel flow). In this paper, the ray analysis is conducted in Fourier space, and required periodic boundary conditions. However, the pulse-type initial conditions considered herein involve extremely long domains, and comparisons with even larger domains are self-consistent. Nevertheless, full numerical simulations would further validate these observations. Such a study and the subsequent non-linear analysis will form the basis of future work.

6.3. Summary

We have studied the linear stability of a liquid layer sheared by laminar or turbulent gas flow in a two-dimensional Cartesian geometry. A Poiseuille (laminar) or Reynolds-averaged (turbulent) model is used to describe the stratified two-phase base flow. Results from a normal-mode analysis and a ray analysis show that the base flow is absolutely unstable to linear perturbations for large regions of parameter space. In particular, for density ratios of $O(1000)$, clear evidence is given of oil/gas flows being absolutely unstable for a sufficiently large dynamic viscosity ratio (at least $O(10^2)$ for the laminar and $O(10^3)$ for the turbulent base state), provided the Reynolds number of the flow is sufficiently high. Since the dynamic viscosity ratio for air/water systems is only $m \approx 55$ at 20°C , the present results for the turbulent case lead us to conclude that laboratory experiments carried out for water/air may not be representative for oil/gas systems.

In both turbulent and laminar base states, the flow-regime map collapses in the (Re, Re_{int}) plane, where Re_{int} is the liquid-based Reynolds number (with a small subset of

exceptional cases). A recently developed theory for C/A transitions (Ó Náraigh *et al.* 2012) has enabled us to formulate a simple criterion for the onset of absolute instability, based on a competition between instability growth and convection by the group velocity. A single number, based on the temporal growth properties, encodes the tendency for instability growth. This number is governed by ϵ , m , and Re , but becomes parameter-free in certain limits, while the behaviour of the group velocity is governed simply by Re_{int} . This criterion therefore explains the importance of Re_{int} in the C/A transition curves, and, moreover, when examined in detail, explains the collapse of the transition curves into universal forms.

Independent confirmation of our results from the modal analysis has been obtained using a ray analysis. The ray analysis benefits from our development of an efficient method of solution for linear differential-algebraic equations, which allows us to extend drastically the simulation time over which the evolution of an initially pulsed disturbance can be traced, thereby eliminating the problems encountered with DNS by Valluri *et al.* (2010). This method all but guarantees the detection of absolute instability, if it exists. Additionally, the ray analysis leads naturally to an energy-budget method that determines the origin of the spatio-temporal instability. Results from this method demonstrate the importance of the viscosity-contrast mechanism acting at the interface, as well as a transfer of energy from the bulk gas flow to the waves, as the sources of the instability. Nevertheless, there exist several internal modes (which also derive energy from the interface) that are at least as significant in other cases. A further application of the ray analysis is envisaged for flows wherein the complex dispersion relation contains singularities (e.g. if $\omega(\alpha)$ has a pole (Healey 2007, 2009) or root-type behaviour (Aships & Reshotko 1990) at some point α_0). In such problems, the application of the saddle-point criterion, with its associated construction of the steepest-descent path enclosing all the dynamically-relevant singularities, is a non-obvious task (Rees & Juniper 2010). For these cases, a straightforward ray analysis could be used to verify the correctness of one's implementation of steepest-descent method. The ray analysis suffers from the amplification of numerical error when the spatial growth rates are large, meaning that only a small region around the impulse centre can be used to extract meaningful information. Thus, both methods are necessary to obtain a complete picture of the stability properties. The ray analysis and the quadratic approximation are quite general, and we anticipate that a wide range of multiphase flow scenarios can be tackled using these techniques.

Appendix A. Validity of the quadratic approximation as applied to the C/A transition of two-phase stratified flow

We review the so-called ‘quadratic approximation’ developed by Ó Náraigh *et al.* (2012) and demonstrate that it approximates well the precise criteria for the onset of absolute instability. The quadratic approximation is based on the following identity for the analytic continuation of the growth rate ω_i into the complex plane:

$$\omega_i(\alpha_r, \alpha_i) = \omega_i^{\text{temp}}(\alpha_r) + \sum_{n=0}^{\infty} \frac{(-1)^n}{(2n+1)!} \frac{d^{2n} c_g}{d\alpha_r^{2n}} \alpha_i^{2n+1} + \sum_{n=0}^{\infty} \frac{(-1)^{n+1}}{(2n+2)!} \frac{d^{2n+2} \omega_i^{\text{temp}}}{d\alpha_r^{2n+2}} \alpha_i^{2n+2}, \quad (\text{A } 1)$$

where c_g is the group velocity $d\omega_r/d\alpha_r$ in a purely temporal analysis. This is a consequence of the Cauchy–Riemann conditions on $\omega(\alpha)$ viewed as a holomorphic function on an appropriate open subset in the complex plane, and has been derived elsewhere by Ó Náraigh *et al.* (2012). We truncate this series at quadratic order in α_i and apply

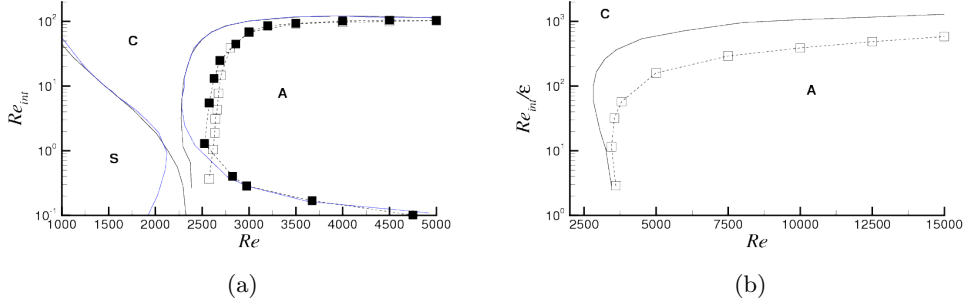


FIGURE 19. Comparison of flow-regime maps resulting from the quadratic approximation (open symbols, keeping m constant; filled symbols, keeping ϵ constant) and the full modal analysis (solid lines) for the turbulent (a) and laminar (b) base state.

the conditions $\partial\omega_i/\partial\alpha_r = \partial\omega_i/\partial\alpha_i = 0$ for a saddle point. This yields the conditions

$$\frac{d\omega_i^{\text{temp}}}{d\alpha_r} + \frac{dc_g}{d\alpha_r}\alpha_i - \frac{1}{2}\frac{d^3\omega_i^{\text{temp}}}{d\alpha_r^3}\alpha_i^2 = 0, \quad c_g(\alpha_r) - \frac{d^2\omega_i^{\text{temp}}}{d\alpha_r^2}\alpha_i = 0. \quad (\text{A } 2)$$

Simultaneous solution of these equations yields the following α_r -value for the location of the saddle point:

$$c_g(\alpha_r)\frac{dc_g}{d\alpha_r} = -\frac{d\omega_i^{\text{temp}}}{d\alpha_r}\frac{d^2\omega_i^{\text{temp}}}{d\alpha_r^2} + \frac{1}{2}c_g^2(\alpha_r)\left(\frac{d^3\omega_i^{\text{temp}}}{d\alpha_r^3}\bigg/\frac{d^2\omega_i^{\text{temp}}}{d\alpha_r^2}\right). \quad (\text{A } 3)$$

(Note that for a strictly quadratic approximation, as in the main part of the paper, the third derivative should be neglected here.) At the onset of absolute instability, $\omega_i = 0$ at the saddle point. Substitution of this condition into the quadratic approximation to Equation (A 1) yields the following criterion for the onset of absolute instability:

$$-\frac{d^2\omega_i^{\text{temp}}}{d\alpha_r^2}\bigg|_{\alpha_r^*}\omega_i^{\text{temp}}(\alpha_r^*) = \frac{1}{2}c_g^2(\alpha_r^*). \quad (\text{A } 4)$$

where α_r^* is the root of Equation (A 3).

In Figure 19, the results of the quadratic approximation are compared with the full modal results that have been taken from Figures 6 and 14 for the turbulent and laminar base states, respectively. All branches are qualitatively correctly predicted, and quantitatively accurate results are even obtained at some, especially all results at large Re in the turbulent case, and those for low Re and a large viscosity ratio in both laminar and turbulent cases.

Appendix B. Analysis of purely spatial modes

The focus throughout the paper has been on spatio-temporal analysis. In particular, our modal analysis has involved the extraction of saddle points from the solution of an eigenvalue problem in a complex wave number space. In this section, we review the Gaster theory for the extraction of purely spatial growth rates. The focus herein is on the turbulent base state.

The most basic description of linear instability is a temporal analysis, which involves the solution of the eigenvalue problem (2.15) for $\alpha = \alpha_r$ only. This gives a dispersion relation $(\omega_r(\alpha_r), \omega_i(\alpha_r))$. The pair $(\omega_r(\alpha_r), \omega_i(\alpha_r))$ that maximizes ω_i is called the *most dangerous temporal mode*. The maximum is taken over the complete spectrum of modes

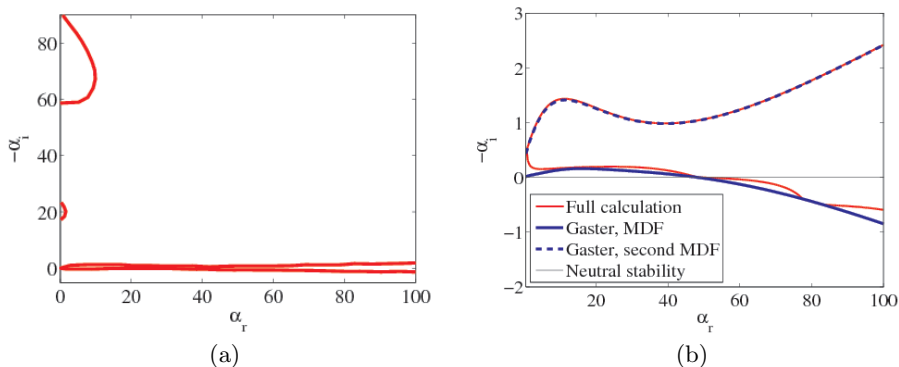


FIGURE 20. (a) Spatial stability study; (b) Comparison with Gaster analysis. Here ‘MDF’ refers to the ‘most-dangerous frequency’, or, equivalently, the most-dangerous mode.

in the linear Orr–Sommerfeld (OS) equations. The system is unstable if $\omega_i > 0$ at the most dangerous temporal mode. This case has been investigated exhaustively by the present authors (Ó Náraigh & Spelt 2010; Ó Náraigh *et al.* 2011*a,b*).

We therefore turn to the spatial case, wherein we are concerned with the dispersion relation $\alpha_i = \alpha_i(\alpha_r, \omega_i = 0)$, which can be obtained by treating the OS problem (2.15) as a non-linear eigenvalue problem in α . In practice, we do not solve this complicated problem. Instead, we solve Equation (2.15) in the complex α -plane, $\alpha := \alpha_r + i\alpha_i$. The result is a discrete spectrum of frequencies $\{\omega_n(\alpha)\}_n$, which we order according to the magnitude of $\Im[\omega_n(\alpha)]$: the *most dangerous mode at complex wave number* α is denoted by $\omega_C(\alpha)$, and is defined such that

$$\Im[\omega_C(\alpha)] = \max_{n, \text{ all modes}} \left\{ \Im[\omega_n(\alpha)] \right\}_{\alpha \in \mathbb{C}}.$$

We plot the zero contour of $\Im[\omega_C(\alpha)] = 0$, which gives the desired relation $\alpha_i = \alpha_i(\alpha_r, \omega_i = 0)$. We repeat these steps for the less dangerous modes. This results in multiple *spatial curves*. These are displayed in Figure 20(a) for the parameter values $m = 55$, $r = 1000$, $\epsilon = 0.05$, with F and S given by Equation (4.1). However, in this figure, we plot only the spatial curves produced by the most dangerous mode; the less dangerous modes do not produce the same large spatial amplification (spatial amplification corresponds to $\alpha_i < 0$), and are not shown. The large spatial growth rates in the figure would appear to dominate in an evolving flow. In practice, however, they are not observed, neither in turbulence nor in laminar flows.

Because the large spatial growth rates are not accessed, we focus our attention on the spatial curves near $\alpha_i = 0$, for which an analytical theory is available. Gaster (1962) has shown that small spatial growth rates are related to the temporal ones through the formula

$$-\alpha_i = \omega_i / \frac{\partial \omega_r}{\partial \alpha_r}, \quad (\text{B } 1)$$

where the quantities on the right-hand side are derived from the purely temporal analysis. We test the applicability of Equation (B 1) in Figure 20(b). We plot the Gaster curves associated with the temporally most dangerous mode and the second most dangerous mode in the figure, and compare the result with the contour in Figure 20(a). There is good agreement between the two theories. However, the curve generated from the contour analysis exhibits ‘kinks’ where the most dangerous mode switches from one eigenmode

to another. To obtain perfect overlap between the two curve sets, it is necessary to pick out all the eigenmodes from the contour analysis and to cut and re-connect the contours so as to obtain smooth curves. This exercise is difficult but yields no new information, and we do not pursue it here. Instead, we focus on the Gaster study, where two spatial curves overlap with the contour-generated ones. The Gaster curves are obtained from the first and second temporally most dangerous modes. Thus, the character of a spatial instability is identified with the character of the temporal instability through the Gaster formula (B1). The Gaster curve suggests that the second most dangerous temporal mode contributes most strongly to the spatial instability. However, it is not obvious from this simple analysis which eigenmode is excited in an impulse-response scenario: this question is studied in detail in Section 5, where it is demonstrated that the spatial curve associated with the temporally most dangerous mode is the one that is selected.

Acknowledgements

The authors would also like to thank J.-C. Loiseau for carrying out preliminary numerical investigations for this project.

REFERENCES

- AR, S. & CAI, J.-Y. 1994 Reliable benchmarks using numerical instability. In *Proceedings of the fifth annual ACM-SIAM Symposium on Discrete Algorithms*.
- ARFKEN, G. B. & WEBER, H. J. 2001 *Mathematical methods for physicists*, 5th edn. Harcourt.
- ASHIPS, D. E. & RESHOTKO, E. 1990 The vibrating ribbon problem revisited. *J. Fluid Mech.* **213**, 531.
- BIBERG, D. 2007 A mathematical model for two-phase stratified turbulent duct flow. *Multiph. Sci. Tech.* **19**, 1.
- BOOMKAMP, P. A. M., BOERSMA, B. J., MIESEN, R. H. M. & v. BELJNON, G. 1997 A Chebyshev collocation method for solving two-phase flow stability problems. *J. Comp. Phys.* **132**, 191.
- BOOMKAMP, P. A. M. & MIESEN, R. H. M. 1996 Classification of instabilities in parallel two-phase flow. *Int. J. Multiphase Flow* **22**, 67.
- BRADSHAW, P. 1974 Possible origin of Prandtl's mixing-length theory. *Nature* **249**, 135.
- CHOMAZ, J.-M. 2005 Global instabilities in spatially developing flows: non-normality and non-linearity. *Ann. Rev. Fluid Mech.* **37**, 357–392.
- COHEN, L. S. & HANRATTY, T. J. 1965 Generation of waves in the concurrent flow of air and a liquid. *A.I.Ch.E. Journal* **11**, 138.
- CRAIK, A. D. D. 1966 Wind-generated waves in thin liquid films. *J. Fluid Mech.* **26**, 369.
- DELBENDE, I. & CHOMAZ, J.-M. 1998 Nonlinear convective/absolute instabilities in parallel two-dimensional wakes. *Phys. Fluids* **10**, 2724–2736.
- DELBENDE, I., CHOMAZ, J.-M. & HUERRE, P. 1998 Absolute/convective instabilities in the Batchelor vortex: a numerical study of the linear impulse response. *J. Fluid Mech.* **355**, 229–254.
- GASTER, M. 1962 A note on the relation between temporally-increasing and spatially-increasing disturbances in hydrodynamic instability. *J. Fluid Mech.* **14**, 222.
- GONDRET, P., ERN, P., MEIGNIN, L. & RABAUD, M. 1999 Experimental evidence of a non-linear transition from convective to absolute instability. *Phys. Rev. Lett.* **82**, 1442–1446.
- HALL-TAYLOR, N. S. & HEWITT, G. F. 1970 *Annular Two-Phase Flows*. Oxford: Pergamon Press.
- HEALEY, J. J. 2007 Enhancing the absolute instability of a boundary layer by adding a far-away plate. *J. Fluid Mech.* **579**, 29.
- HEALEY, J. J. 2009 Destabilizing effects of confinement on homogeneous mixing layers. *J. Fluid Mech.* **623**, 241.
- HOOGENDOORN, C.J. 1959 Gas-liquid flow in horizontal pipes. *Chem. Eng. Sci.* **9**, 205–217.

- HUERRE, P. & MONKEWITZ, P. A. 1990 Local and global instability in spatially developing flows. *Ann. Rev. Fluid Mech.* **22**, 473–537.
- LECOEUR, N., HALE, C. P., SPELT, P. D. M. & HEWITT, G. F. 2010 Visualization of droplet entrainment in turbulent stratified pipe flow. In *7th International Conference on Multiphase Flow ICMF 2010*.
- LINGWOOD, R. J. 1997 On the application of the Briggs' and steepest-descent methods to a boundary-layer flow. *Studies in Applied Mathematics* **98**, 213.
- MANDANE, J.M., GREGORY, G.A. & AZIZ, K. 1974 A flow pattern map for gas-liquid flow in horizontal pipes. *Intl J. Multiph. Flow* **1**, 537–553.
- MIESEN, R. & BOERSMA, B. J. 1995 Hydrodynamic stability of a sheared liquid film. *J. Fluid Mech.* **301**, 175.
- MILES, J. W. 1957 On the generation of surface waves by shear flows. *J. Fluid Mech.* **3**, 185.
- MONIN, A. S. & YAGLOM, A. M. 1971 *Statistical Fluid Mechanics: Mechanics of Turbulence*. Cambridge, MA: MIT Press.
- ÖZGEN, S., DEGREG, G. & SARMA, G. S. R. 1998 Two-fluid boundary layer stability. *Phys. Fluids* **10**, 2746.
- POPE, S. B. 2000 *Turbulent Flows*. Cambridge, UK: Cambridge University Press.
- REES, S. J. & JUNIPER, M. P. 2010 The effect of confinement on the stability of viscous planar jets and wakes. *J. Fluid Mech.* **656**, 309.
- SHAMPINE, L. F., REICHEL, M. W. & KIERZENKA, J. A. 1999 Solving Index-I DAEs in MATLAB and Simulink. *SIAM Review* **41**, 538.
- Ó NÁRAIGH, L. & SPELT, P. D. M. 2010 Interfacial instability of turbulent two-phase stratified flow: Pressure-driven flow and non-Newtonian layers. *J. Non-Newt. Fluid Mech.* **165**, 489 – 508.
- Ó NÁRAIGH, L., SPELT, P. D. M., MATAR, O. K. & ZAKI, T. A. 2011*a* Interfacial instability of turbulent two-phase stratified flow: Pressure-driven flow and thin liquid films. *Int. J. Multiph. Flow* **37**, 812 – 830.
- Ó NÁRAIGH, L., SPELT, P. D. M. & SHAW, S. J. 2012 An analytical connection between temporal and spatio-temporal growth rates in linear stability analysis. Eprint: arXiv:1203.1797v1.
- Ó NÁRAIGH, L., SPELT, P. D. M. & ZAKI, T. A. 2011*b* Turbulent flow over a liquid layer revisited: multi-equation turbulence modelling. *J. Fluid Mech.* **683**, 357 – 394.
- VALLURI, P., Ó NÁRAIGH, L., DING, H. & SPELT, P. D. M. 2010 Linear and nonlinear spatio-temporal instability in laminar two-layer flows. *J. Fluid Mech.* **656**, 458–480.
- YIH, C. S. 1967 Instability due to viscosity stratification. *J. Fluid Mech.* **27**, 337.